RES | THE SCHOOL for RENEWABLE ENERGY SCIENCE

Internal Reforming and Mass Transport Properties of a Reaction Sintered Ni-YSZ and a Novel Porous Metal Support for SOFC Applications.

Michael G. McNeeley

UNIVERSITY OF ICELAND

University of Akureyri

Internal Reforming and Mass Transport Properties of a Reaction Sintered Ni-YSZ and a Novel Porous Metal Support for SOFC Applications.

Michael G. McNeeley

A 30 ECTS credit units Master´s thesis

Advisor:

Dr. Neal Sullivan

Assistant Professor: Colorado School of Mines, Department of Engineering

Director: Colorado Fuel Cell Center

A Master´s thesis done at

RES | The School for Renewable Energy Science

in affiliation with

University of Iceland &

University of Akureyri

Akureyri, February 2011

Internal Reforming and Mass Transport Properties of a Reaction Sintered Ni-YSZ and a Novel Porous Metal Support for SOFC Applications.

A 30 ECTS credit units Master´s thesis

RES | The School for Renewable Energy Science

Solborg at Nordurslod

IS600 Akureyri, Iceland

Telephone + 354 464 0100

www.res.is

Printed in (date)

at Stell Printing in Akureyri, Iceland

ABSTRACT

High temperature solid oxide fuel cells have the capability of reforming conventional hydrocarbon fuels into hydrogen directly within the fuel cell anode itself. These systems can achieve efficiencies much greater than current electricity generation techniques using the combustion of fuel. The design of a high performing internal reforming SOFC system is extremely challenging because the anode must function as both fuel reformer and electrochemical anode. The risk of carbon formation in the anode structure itself is a serious concern because the reforming environment is coupled to both reforming activity and the electrochemical activity of the anode. Anode materials must be carefully engineered to perform in this environment.

SOFC systems are currently limited by their dependence on ceramic cell components. The use of these components prevents rapid thermal cycling of the SOFC systems giving them poor rapid start up and load following capabilities. To help alleviate these issues, SOFCs using a metal support are being developed. Internal reforming metal supported SOFC systems are extremely well suited for both mobile auxiliary power units and stationary backup power systems, due to their enhanced thermal cycling capabilities.

Utilizing the unique Separated Anode Experiment at the Colorado School of Mines the internal reforming and mass transport characteristics of a conventional ceramic anode and a porous metal support are evaluated independent of electrochemical operation. This experiment provides analysis of the anode morphology and how it affects species transport through the structure. These results provide insight to the future design efforts for both ceramic and metal supported SOFC system.

PREFACE

This thesis is made on the topic of mass transport and internal reforming kinetics of SOFC anodes and supports. It is prepared by the author to satisfy the graduation requirements for a M.Sc. degree in Renewable Energy Science from RES| The School for Renewable Energy Science. RES is a joint graduate program between the University of Iceland in Reykjavik Iceland and the University of Akureyri in Akureyri Iceland. All work detailed in this report was conducted between October 2010 and February 2011, while in residence at the Colorado Fuel Cell Center at the Colorado School of Mines in Golden Colorado. The advisor for this project was Dr. Neal Sullivan asst. professor of Engineering at the Colorado School of Mines and director of the Colorado Fuel Cell Center. This thesis was defended before a University of Iceland and University of Akureyri approved defense committee on February 10, 2011 at Nýsköpunarmiðstöð Íslands (Icelandic Center of Innovation) in Reykjavik. Members of the thesis defence committee were; Dr. Þorsteinn Ingi Sigfusson, professor of Physics at the University of Iceland, director general of the Icelandic Center of Innovation, coordinator of Hydrogen Systems and Fuel Cells concentration at RES| The School for Renewable Energy Science; Dr. David Dvorak, professor of Mechanical Engineering Technology at University of Maine, coordinator of Hydrogen Systems and Fuel Cells concentration at RES| The School for Renewable Energy Science; Dr. Neal Sullivan asst. professor of Engineering at the Colorado School of Mines and director of the Colorado Fuel Cell Center; and Dr. Guðmundur Gunnarsson of the Icelandic Center of Innovation, as examiner.

This work was prepared solely by the author and constitutes an original scientific work; however, like all scientific work, this thesis is possible only because of the previous work of others. All efforts were made to reference and cite all works that contributed directly to the writing of this thesis.

ACKNOWLEDGEMENTS

There are several entities that I would like to thank for assisting me with this thesis and over the course of my studies. I would like to thank the RES administration and staff for their assistance throughout this year in Iceland and the universities of Iceland and Akureyri for providing academic and facility support for the RES program. This research was conducted at the Colorado Fuel Cell Center at the Colorado School of Mines. I am thankful and appreciative for the facilities and support provided by the CFCC and CSM. Finally I would like to thank Plansee SE for supplying the ITM samples used in this work.

I received assistance from several individuals while conducting my research. I would like to thank; Shaun Babiniec for his ceramics expertise and sample preparation; Nicolaus Faino, Gary Zito, and John Chandler for assistance with the SEM work; Professor Robert Kee for his modeling background and illustrations used extensively in this report; Guðmundur Gunnarsson for his participation on my defense committee as examiner, The Hydrogen Systems and Fuel Cells concentration coordinators Þorsteinn Sigfusson and David Dvorak for their guidance, suggestions and logistical support; and Amber Waite and Mike Lindemann for their editing assistance and useful feedback.

Two people, above all others, worked with me to insure the high academic quality of this work, my advisor Dr. Neal Sullivan and PhD. candidate Amy Richards, both at the CFCC. Dr. Sullivan was instrumental in securing the samples used, securing financial support, and academic support for this work. He is a talented and dedicated educator who values his students and wants to see them all succeed. Amy Richards has worked on the SAE apparatus and computational model used in this work for over two years as a graduate student at CSM. Her years of effort have made the SAE a highly repeatable and effective experiment. In many ways Amy acted as a second advisor for this project and without her and her expertise, this thesis would not have been possible.

Finally, I would like to dedicate this work to my parents, Mike and Alda McNeeley, and my wonderful girlfriend, Amber Waite. Their undying and unconditional support has been the pillar that I have leaned on throughout this experience.

TABLE OF CONTENTS

LIST OF FIGURES

LIST OF TABLES

LIST OF ABBREVIATIONS

AFC.....Alkaline fuel cell

AFL.....Anode functional layer

ASR.....Area specific resistance

AT.....Auto thermal reforming

CAA.....Catalytic active area

CFCC.....Colorado Fuel Cell Center

CGO.....Gadolinium-doped ceria

CPOX.....Catalytic partial oxidation reforming

CSM.....Colorado School of Mines

CTE.....Coefficient of thermal expansion

DBL.....Diffusion barrier layer

DGM.....Dusty Gas Model

DIR.....Direct internal reforming

DMFC.....Direct methanol fuel cell

DR.....Dry reforming

EDX.....Energy-dispersive X-ray spectroscopy

EIS.....Electrochemical impedance spectroscopy

FC.....Fuel cell

GC.....Gas chromatograph

HC.....Hydrocarbon

HTFC.....High temperature fuel cell

IIR.....Indirect internal reforming

IT-SOFC.....Intermediate temperature solid oxide fuel cell

LSCM.....$La_{0.5}Sr_{0.25}Cr_{0.97}Ma_{0.03}O_3$

LSM.....$La_{0.5}Sr_{0.5}MnO_3$

LSSM..... $La_{0.8}Sr_{0.2}Mn_{0.8}O_3$

LSVC.....$La_{0.5}Sr_{0.25}Cr_{0.97}V_{0.03}O_3$

LTFC.....Low temperature fuel cell

MCFC.....Molten carbonate fuel cell

MFC.....Mass flow controller

Ni-YSZ.....Nickel-doped yttria stabilized zirconia

ODS.....Oxide dispersive strengthened

PAFC.....Phosphoric acid fuel cell

PC.....Personal computer

PEMFC.....Proton exchange membrane fuel cell

PM.....Powder metallurgy

POX.....Partial oxidation reforming

RWGS.....Reverse water gas shift reaction

SAE.....Separated anode experiment

S/C.....Steam to carbon ratio

ScSZ.....Scandia stabilized zirconia

SDC.....Samaria-doped ceria

SOFC.....Solid oxide fuel cell

SR.....Steam reforming

TC.....Total carbon

TPB.....Triple phase boundary

WGS.....Water gas shift reaction

XRD.....X-Ray diffraction

YSZ.....Yttria stabilized zirconia

LIST OF SYMBOLS

j_0……..……...Exchange current density

n……Number of electrons exchanged during reaction

F…….……..Faraday's constant

f_1……..Reactant decay rate

R…….…...……...……..Universal gas constant

T……..…….…….……Temperature

c_R^* ……...…….……..Reactant concentration

$\Delta G_1^{\ddagger}$ ……..……...…….……Activation barrier for reaction

n_x ……..……...……Moles of subscripted species

E^0.....Standard electrode potential

$a_x^{v_i}$ ……...……..…….Chemical activity of subscripted species

$v_{open}^{\%}$ ……..……..…….Volume percentage of open porosity

m_x …….…….……mass of subscripted object

$\dot{m}^{\ddagger}$ .....Mass flow out of x direction channel

$\dot{m}_k$ .....Mass flow into x direction channel element

j_k^c .....Mass flux of the subscripted species in the z direction

A_c .....cross sectional area element at the manifold and SAE sample

Y_k.....subscripted species mass fraction

A_s.....specific area

$\dot{s}_k$ .....Molar production rate of subscripted species

W_k.....Molecular weight of subscripted species

J_k.....Molar flux of subscripted species

$[X_k]$.....Molar concentration of subscripted species

p.....Pressure gradient

B_g.....Permeability

μ.....Mixture viscosity

ρ.....pressure within the sample

P.....Pressure

$\bar{W}$ .....Average molecular weight

1 INTRODUCTION

A fuel cell (FC) is an electrochemical device that directly converts chemical fuel into electricity. Conventional electricity generation techniques typically combust fuel to produce mechanical work which is then converted into electricity. These processes use thermodynamic cycles of a working fluid and are therefore limited by the Carnot efficiency. Fuel cells on the other hand, directly convert the chemical energy in the fuel stream into electricity. Since the fuel is directly converted to electricity via electrochemical reactions there is no thermodynamic cycle. As such, the fuel cell is not limited by the Carnot efficiency and is therefore capable of running at higher efficiencies than conventional fuel-based electricity generation technologies.

There are multiple types of fuel cells; however, all fuel cells operate on the same general electrochemical processes. High energy electron bonds in reactant fuels and oxidizers are converted into lower energy bonds in the resulting products of the chemical reaction. The balance of energy from the electrochemical reaction is then released in the form of heat, phase state of the products, and electricity. The chemical reaction of fuel and oxidizer is conducted through the transfer of electrons from the fuel (oxidation) to the oxidizer (reduction). By intercepting the electrons during the transfer and forcing them through an external circuit, energy in the form of electricity can be directly extracted from the chemical reaction.

In order to capture the electrons from the chemical reaction, the fuel and oxidizer must be physically separated by a membrane placed between two electrodes, an anode and a cathode. The membrane allows the transmission of reactant ions while inhibiting the transmission of electrons. The electrodes host the electrochemical reactions and act as electron collectors and conductors. The electrode where the electrochemical fuel is oxidized is the anode. The electrode where the oxidizer is reduced is the cathode. The membrane separating the anode and the cathode is referred to as the electrolyte. The electrolyte has the unique properties of conducting ions (either positive or negative, depending on the fuel cell type) but having zero electronic conductivity. The electrolyte's resistance to electron flow results in a build-up of electrons in the anode and positive ion build-up in the cathode, which leads to an electrical potential. This electrical potential can then force electrons through an external circuit similar to a battery.

1.1 Types of fuel cell

While there are numerous differences amongst the various forms of fuel cells, all major types of fuel cells can be classified into two general classes by operating temperature, high temperature fuel cells (HTFC), and low temperature fuel cells (LTFC). In general, low temperature FCs operate in the temperature range of 60C to 250C while high temperature fuel cells operate from 400C – 1200C. The low temperature classification includes; Proton Exchange Membrane (PEMFC), Phosphoric Acid (PAFC), Direct Methanol (DMFC) and Alkaline (AFC) fuel cell types while the high temperature classification includes Molten Carbonate (MCFC) and Solid Oxide (SOFC) fuel cell types. Generally LTFCs have the advantage of quick response to transient electrical demand while suffering from increased fuel incompatibility and/ or catalyst poisoning issues. HTFCs on the other hand benefit from increased fuel flexibility and poison tolerance but have a generally poor response time to transient electrical load dynamics.

1.2 The role of catalysts

The rate of the electrochemical reaction within the fuel cell can be characterized by the exchange current density as seen in equation 1.1 below(R. O'Hayre, 2008).

$$j_0 = nF\, c_R^* f_1 e^{-\Delta G_1^{\ddagger}/(RT)} \tag{1.1}$$

Where n is the number of electrons transferred in the reaction, F is the Faraday constant , c_R^* is the reactant concentration, f_1 is the decay rate of the reactant, $\Delta G_1^{\ddagger}$ is the activation barrier for the reaction, R is the universal gas constant, and T is the temperature.

It can be seen from equation 1.1 that by decreasing the activation barrier ($\Delta G_1^{\ddagger}$) of the reaction the exchange current density will increase, and therefore the rate of the reaction will increase. Catalysts are introduced into both the fuel cell anode and cathode to lower the activation barrier to the hydrogen oxidation and oxygen reduction reactions. The highest performing catalysts for this purpose are the transition metals surrounding the platinum group, with platinum (Pt) itself showing the best performance. For this reason, Pt tends to be the main catalyst of choice for LTFCs. By examining equation 1.1 it can be seen that increasing the operating temperature of

the fuel cell will also lead to an increase in the reaction rate. Due to the increased reaction kinetics within the high temperature fuel cells they can utilize less active catalysts like nickel (Ni). This is a distinct advantage because Ni is much cheaper than Pt.

The chemical reaction within the fuel cell can only take place where reactant ions and electrons can combine. This can only occur in a region where the catalyst, fuel bearing gas, and reactant ion conducting electrolyte meet. This region is known as the triple phase boundary (TPB). In equation 1.1 the exchange current within the fuel cell is expressed as a current density. As such, the overall exchange current in the fuel cell is highly dependent on the total surface area accessible to the reaction. In order to maximize fuel cell performance the catalyst loading and the TPB surface area at the electrode-electrolyte interface should be maximized.

1.3 Fuel requirements

All major types of fuel cells are either directly or indirectly dependent on hydrogen as a fuel and oxygen as an oxidizer. Hydrogen is either sent to the fuel cell directly or via a "hydrogen carrier" that receives further processing in the fuel cell system to extract the hydrogen. Examples of common hydrogen carriers are hydrocarbon fuels like methane or alcohols such as methanol.

The presence of catalysts in the fuel cell electrodes make them intolerant to various contaminants that are common in the conventional hydrogen carriers. Chemical contaminates in the fuel supply of a fuel cell leads to deactivation of the catalysts present in the anode through chemical "poisoning" which increases the activation losses in the FC and decreases system efficiency. Catalyst deactivation can eventually lead to cell death. In LTFCs Pt is often used as a catalyst for the hydrogen oxidation reaction in the anode. Pt is susceptible to poisoning from sulfur (S) compounds and carbon monoxide (CO). S and CO form a strong chemical bond with Pt. Once the Pt atom has formed a chemical bond it is rendered inert and no longer functions as an oxidation catalyst for hydrogen. The poisoning of the catalyst present in the anode results in a reduction of its catalytic activity, because the total number of available reaction sites at the TPB has been reduced.

HTFCs such as SOFCs typically use Ni as the catalyst for the hydrogen oxidation reaction. Ni based catalysts in SOFCs are tolerant of CO contaminates in the fuel stream because CO does not form a strong chemical bond with Ni at the operation temperatures typical of these systems. For HTFCs, CO can actually act as a fuel by reacting with product water in the FC anode to

form additional H_2 fuel via the water gas shift reaction or by being chemically oxidized to CO_2 directly, which is discussed in section 1.4 of this paper. Nickel based catalysts; however, remain intolerant to S compounds because Ni and S form a strong bond similar to Pt. While the HTFC's Ni based catalysts are deactivated by S compounds, they can tolerate S concentrations as high as 1ppm while Pt based LTFCs can only tolerate up to approximately 0.1ppm (Song, 2002).

1.4 Fuel reforming

As discussed in section 1.3, essentially all fuel types require H_2 fuel, either directly or indirectly. Hydrogen, unfortunately, is not the most convenient fuel. While H_2 is the most abundant element in the universe, it does not occur in its elemental form naturally on Earth (Jefferson Lab, 2010). Therefore all pure hydrogen that would be used for fuel in fuel cell systems must first be generated by processing available hydrogen containing compounds, most commonly water (H_2O) and various hydrocarbons. The generation of H_2 from a hydrocarbon (HC) feed stock is commonly referred to as a reforming process. There are four main types of reforming processes that are relevant to fuel cell systems; steam reforming, partial oxidation reforming, auto thermal reforming, and dry reforming.

1.4.1 Steam reforming

Hydrocarbon steam reforming (SR) is currently the most common form of H_2 production on the planet (United States Department of Energy, 2008). In the SR reaction a stream of gaseous HC fuel is reacted with gaseous water (steam) to form CO and H_2 gases. Refer to equation 1.2 for the SR reaction for methane gas (CH_4) (Song, 2002). The general SR reaction for any HC feed stock is shown in equation 1.3(Song, 2002).

$$CH_4 + H_2O \rightarrow CO + 3H_2 \tag{1.2}$$

$$C_mH_n + mH_2O = mCO + (m + (\frac{1}{2})n)H_2 \tag{1.3}$$

Steam reforming is a highly endothermic reaction and therefore requires a large amount of thermal energy for the reaction to occur. Normal temperature range for SR is from 700-1000 C. In order to maximize H_2 production more steam than is required by the stoichiometry is supplied to the reaction. The increase in the concentration of H_2O forces the chemical equilibrium to favour the products via Le Chatelier's Principle (R. O'Hayre, 2008). The steam-to-carbon ratio (S/C) is commonly used to describe the relative concentration of water to fuel. The S/C is shown in equation 1.4 below where n_{H_2O} is the number of moles of steam present and n_c is the number of moles of atomic carbon present at the reaction site.

$$\frac{S}{C} = \frac{n_{H_2O}}{n_c} \tag{1.4}$$

Catalysts are employed to aid the SR reaction by decreasing the activation barrier of the reaction. Various transition metals are commonly used as catalysts for the steam reforming reaction. The catalyst used can vary greatly based on the HC feedstock and operating conditions within the reactor. However, both Pt and Ni are commonly used as reforming catalysts (K. Tomishige, 2004). As discussed earlier, these two catalysts are also commonly used as catalysts for the H_2 oxidation reaction in fuel cell anodes.

1.4.2 Partial oxidation reforming

While the steam reforming reaction has high H_2 yield, its high energy requirement makes it somewhat impractical for either small scale or low temperature systems. Hydrogen generation from HC feed stock is also possible though partial oxidation reforming (POX). POX occurs when HC feedstock is reacted with a sub-stoichiometric amount of O_2. The term "partial oxidation" comes from the fact that the products of the reaction are only partially oxidized. The POX reaction is an exothermic reaction and thus does not require energy from the environment to react, making this type of reforming attractive to small scale and/or low temperature systems. Like the SR reaction the POX reaction is often performed in the presence of catalysts, in this case the reaction is referred to as Catalytic Partial Oxidation (CPOX). The chemical equation for the partial oxidation of CH_4 can be seen below in equation 1.5 (Song, 2002). Equation 1.6 is the general equation for partial oxidation of any HC feed stock (Song, 2002).

$$CH_4 + O_2 \rightarrow CO + 2H_2 \quad (1.5)$$

$$C_mH_n + (\frac{1}{2})mO_2 \rightarrow mCO + (\frac{1}{2})nH_2 \quad (1.6)$$

1.4.3 Water gas shift

The water gas shift (WGS) reaction is an exothermic reaction of CO and gaseous H_2O to form H_2 and CO_2. For fuel cell systems the WGS reaction is rarely employed as a standalone reforming reaction it is generally employed as a secondary reaction to the SR or CPOX reactions. By using the product CO from the SR or CPOX reaction and excess steam in the system the WGS reaction can increase H_2 yield of a reforming process by approximately 5%(R. O'Hayre, 2008). The WGS reaction is shown in equation 1.7 below(Song, 2002).

$$CO + H_2O \rightarrow CO_2 + H_2 \quad (1.7)$$

1.4.4 Autothermal reforming

Autothermal reforming combines the endothermic SR reaction with the exothermic CPOX reaction into a single reforming process. The two reactions are often combined with the addition of a WGS reaction in a thermo-neutral manner; such that the energy requirements of the SR reaction are met by the energy produced in the CPOX reaction. It is important to note the thermo-neutral aspect of this process pertains purely to the reaction energies themselves and not the energy required to heat the reactants to the reaction temperature, which can be a significant thermal load. The CH_4 specific autothermal reaction is shown in equation 1.8 (Song, 2002). While the general reaction for any HC feed stock is shown in equation 1.9 (Song, 2002).

$$CH_4 + \frac{1}{2}O_2 + \frac{1}{2}H_2O \rightarrow CO + \frac{5}{2}H_2 \quad (1.8)$$

$$C_mH_n + (\frac{1}{2})mH_2O + (\frac{1}{4})mO_2 \rightarrow mCO + ((\frac{1}{2})m + (\frac{1}{2})n)H_2 \quad (1.9)$$

1.4.5 CO_2 dry reforming

Dry reforming (DR) is the process of reforming a HC feedstock by reacting it with CO_2 gas at a high temperature as described by the chemical equation below (equation 1.10) (E. Ruckenstein, 1995).

$$CH_4 + CO_2 \rightarrow 2CO + 2H_2 \tag{1.10}$$

DR is rarely employed as a standalone reforming method when H_2 production is the goal of the process because the energy requirements of the DR reaction are higher than the energy required for the SR reaction and H_2 yield from the DR reaction is lower than that of the SR reaction. The DR reaction is, however, employed when reformate gas is to be used as synthesis gas (H_2 + CO) for Fischer-Tropsch syntheses or similar processes. This is because the DR reaction has a higher selectivity to CO and the lower H_2/CO ratio of the reaction is more conducive for the subsequent reactions necessary for synthetic fuel production (E. Ruckenstein, 1995). The DR reaction is also more prone to carbon formation than SR, which is discussed in the next section.

1.4.6 Carbon formation

When reforming a HC feedstock into H_2 care must be taken to avoid the formation of elemental carbon during the process. Carbon formation is often referred to as coking. Elemental carbon is a solid at high temperatures and its formation in the reaction chamber can lead to deactivation of the reforming catalyst and reduction of the gas diffusion in the chamber which significantly retards the reforming reaction and decreases H_2 yield. For CH_4 reforming coking can occur via three main reactions; methane decomposition (equation 1.11), The Boudouard reaction (equation 1.12), and a form of the reverse water gas shift reaction (equation 1.13) (E. Ruckenstein, 1995) ,(H. Sumi, 2010).

$$CH_4 \rightarrow C + 2H_2 \quad (1.11)$$

$$2CO \rightarrow C + CO_2 \quad (1.12)$$

$$H_2 + CO \rightarrow C + H_2O \quad (1.13)$$

Many factors are involved in carbon formation during a reforming process; such as, operating temperature, material composition and morphology of the reactant chamber, feedstock composition, reforming catalyst used, and reforming reactant stoichiometry. Hei, Chen etal. and Rostup-Nielsen and Hansen have published separate papers documenting the reforming characteristics of transition metal catalysts both suggesting that the choice of catalyst plays a key role in the carbon formation during the reforming reaction (J.R. Rostrup-Nielsen, 1993),(M.J. Hei, 1998) . In general higher hydrocarbon fuels have higher propensities for coking as well (J.R. Rostrup-Nielsen, 1993). Carbon formation during the reforming process can also be minimized by running steam to carbon or CO_2 to carbon ratios greater than one in the case of the SR or DR reactions respectfully. Unfortunately running additional reforming reactants decreases overall system efficiency (H. Sumi, 2010).

1.5 Fuel reforming systems

To avoid practicality issues associated with hydrogen fuel, manufactures of fuel cell systems often design onboard fuel reforming systems that allow the fuel cell to operate on more widely available fuels like methane or propane. Inclusion of these reforming systems greatly increases the fuel flexibility of the fuel cell system, which in turn eases integration issues into existing systems; for example, the use of fuel cells as auxiliary power units in transportation where the fuel cell system can operate on the same fuel as the propulsion system.

1.5.1 External reforming systems

External reforming fuel cell systems are fuel cell systems that are dependent on an external reforming subsystem for their supply of hydrogen fuel. External fuel reforming subsystems can either be located in close proximity to the fuel cell system itself or linked to the fuel cell via pipelines. Low temperature PEM or Alkaline fuel cells typically use CPOX or AT external fuel reforming subsystems because the operating temperatures of those systems pose poor thermal integration potential for highly endothermic reforming reactions like steam reforming. For high

temperature systems like SOFCs external reforming systems are typically in close thermal contact with the fuel cell stack. The use of the high quality heat from the stack can support the highly endothermic, but high yielding, steam reforming reaction. Use of the waste heat from the stack for the reforming of HC fuel greatly increases overall system efficiency.

1.5.2 Internal reforming systems

Fuel cell systems that are capable of reforming HC fuel into H_2 within the fuel cell stack itself are referred to as internal reforming fuel cell systems. The reforming reaction can occur in the anode structure itself or prior to reaching the actual anode by reforming within the gas distribution channel of the stack interconnect plates. Fuel cell systems where HC reforming is performed prior to the reaching the anode are referred to as indirect internal reforming systems (IIR). Systems where the HC fuel is reformed within the anode itself are referred as direct internal reforming systems (DIR). High temperature fuel cells are currently the only fuel cell systems that have internal reforming capabilities because their high operating temperatures can support highly endothermic reforming reactions like steam reforming. In addition high temperature fuel cells are more tolerant of fuel contaminates typically present in the HC feedstock (CO) so there is less of a need to purify the reformate (assuming the fuel is low in sulfur content).

1.6 The SOFC

There are multiple types of fuel cells and while they all operate on the same general principles, each type of fuel cell has its own mode of operation and operating temperature. One of the most promising fuel cell types is the solid oxide fuel cell (SOFC). The general operating temperature range for a SOFC system is from 400C-1000C. The SOFC category can be divided into two subgroups by operating temperature. Intermediate temperature solid oxide fuel cells (IT-SOFC) operate in a temperature range of 400-800C and high temperature SOFCS operate from 800-1000C. The high operating temperature of SOFC systems pose unique material challenges. The extreme SOFC environment rapidly degrades common materials. Ceramics are commonly used in place of metals as most metal alloys cannot withstand the high heat and degrade quickly. Commonly used sealants will not work at such high temperatures so ceramic based pastes or glass seals are often used; however, they are brittle and do not tolerate expansion and contraction associated with thermal cycling of the system. The high operating temperature of the SOFC leads to advantages as well. It allows for high electrochemical

efficiency while using cheaper, less active catalysts like Ni. The high operating temperature also provides increased fuel flexibility through increased contaminate tolerance and the ability to support internal reforming of HC fuels. The high temperature also provides excellent prospects for combined heat and power applications.

1.6.1 SOFC operation

SOFCs, like the other major types of fuel cells, operate based on the simple hydrogen combustion reaction below equation (1.14).

$$H_2 + 2O_2 \rightarrow H_2O \tag{1.14}$$

However in the case of a fuel cell the hydrogen and oxygen are separated by an electrolyte. It is useful to consider the above complete combustion reaction as the sum of two half-reactions, the oxidation (loss of electrons) of hydrogen (equation 1.15) and the reduction (gain of electrons) of oxygen (equation 1.16). The oxidation of the hydrogen fuel occurs in the anode and the reduction of the oxygen occurs in the cathode.

$$H_2 + O^{2-} \rightarrow H_2O + 2e^- \tag{1.15}$$

$$\frac{1}{2}O_2 + 2e^- \rightarrow O^{2-} \tag{1.16}$$

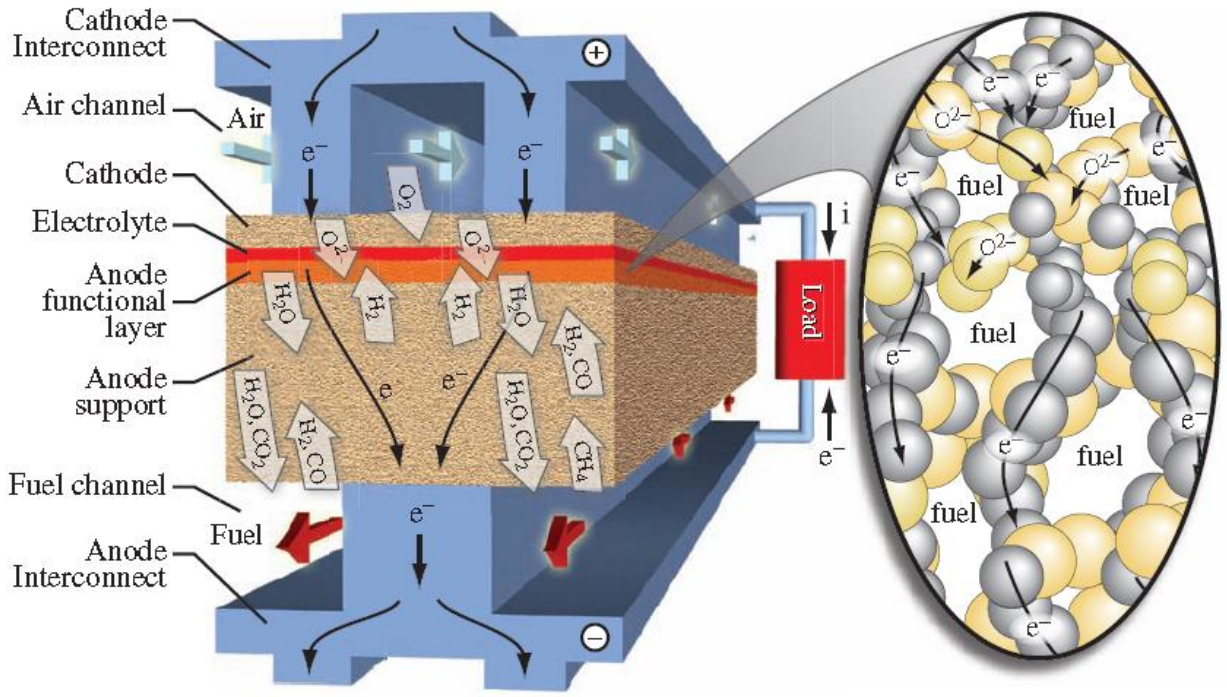

Figure 1- Diagram of internal reforming SOFC processes. Inset shows triple phase boundary at the anode electrolyte interface. Diagram taken from (E. Hecht, 2005)

Figure 1 shows a diagram of SOFC operation. On the cathode side, oxygen diffuses from the channel through the cathode structure. The O-O bond of the O_2 molecule, in a surface reaction with the catalyst present, is weakened and the molecule is absorbed onto the surface of the cathode (chemisorption). Once the O atoms are absorbed onto the cathode surface they are electrochemically reduced into O^{2-} ions by reacting with electrons arriving from an external load. Equation 1.17 provides a better description of the oxygen reduction reaction.

$$(O_2 \xrightarrow{catalyst} 2O) + 4e^{-} \xrightarrow{ext.load} 2O^{2-} \qquad (1.17)$$

Once reduced, the oxygen ions are conducted through the ion conducting electrolyte where they react with the hydrogen fuel to form water and electrons at the anode electrolyte barrier (equation 1.15).

The electrons are sent from the anode to the cathode through an external load where the electrical energy is harvested. In order for the hydrogen fuel to react with the O^{2-} ions the

hydrogen molecule must be dissociated by the catalyst and absorbed onto the surface of the anode, similar to the oxygen dissociation in the cathode. The dissociated hydrogen atoms are now lightly bonded to the catalyst surface where they react with the arriving O^{2-} ions. When the hydrogen atoms and O^{2-} ion react, H_2O is formed and leaves the surface of the anode in a gaseous phase. The electrons from the O^{2-} ion remain bound to the electrode surface and are conducted away to the external load. Below equation 1.18 more aptly describes the reaction occurring at the anode electrolyte interface.

$$(H_2 \overset{catalyst}{\rightarrow} 2H) + O^{2-} \overset{electrolyte}{\rightarrow} H_2O + 2e^- \overset{ext.load}{} \tag{1.18}$$

The steam that is produced at the TPB diffuses back through the anode and is available to support internal SR reaction (equation 1.2)

$$CH_4 + H_2O \rightarrow CO + 3H_2 \tag{1.2}$$

The CO produced during the SR reaction can then react with the water present in the anode to form additional H_2 and CO_2 via the WGS reaction (equation 1.7). Or it can be directly oxidized in to CO_2 at the TPB (equation 1.20)

$$CO + H_2O \rightarrow CO_2 + H_2 \tag{1.7}$$

$$CO + O^{2-} \rightarrow CO_2 + 2e^- \tag{1.20}$$

It is then possible for the CO_2 produced to participate in dry reforming (DR) of the methane (equation 1.10).

$$CH_4 + CO_2 \rightarrow 2CO + 2H_2 \tag{1.10}$$

DR is also likely to take place if the HC fuel is rich in CO_2, for example in the case of bio gas use.

The electrochemical reactions within a fuel cell are complicated and joint optimization of the reforming and electrochemical reactions is a difficult, multifaceted problem, not only due to the electrochemistry, but due to mass transport and reforming kinetics within the fuel cell as well.

Control of the concentration levels of the reforming reactants CO_2 and H_2O present in the anode environment is critical to avoid carbon deposition and fuel starvation issues. Both of these reactants are dependent on both the native fuel composition and operational current density of the fuel cell itself. Since the operational current density of a fuel cell system tends to fluctuate based on usage profile, concentration levels of these reactants tends to fluctuate as well. If there are insufficient amounts of the reforming reactants present, carbon formation in the anode is much more likely occur. However if there is too much steam present in the anode of the fuel cell, the fuel concentration is diluted, which lowers system efficiency. Optimized anode design is critical to balance these issues.

1.7 Objective

Optimization of the anodic function within a fuel cell is critical for system efficiency, reliability, and cost. The processes that occur in an SOFC anode are complicated, multifaceted, and coupled to each other. Hydrogen oxidation reactions, ionic and electronic conduction, fuel reforming, and mass transport of fuel and exhaust all occur in the fuel cell anode simultaneously, and are all coupled to one another. As a result, it is incredibly difficult to predict, and therefore difficult to optimize the performance of an anode. Typically, anode performance is measured indirectly by using electrochemical tests like polarization measurements or electrochemical impedance spectroscopy (EIS) (R. O'Hayre, 2008). These tests measure activity in the entire active cell structure and as a result specific aspects of anodic performance must be inferred from the electrochemical results.

Critical anodic processes like internal reforming and gas transport can be easily masked in electrochemical based tests. The objective of this work is to decouple these critical anodic processes and provide an alternative method for anodic performance assessment and optimization. Through the use of a unique experiment developed by the Colorado Fuel Cell Center (CFCC) it is possible to analyze and measure the critical anodic processes of mass transport and internal reforming performance without the need for electrochemical activity

within the fuel cell. This experiment will be used to demonstrate how easy it is to compare two drastically different anode structures and help predict their transport and reforming performance in SOFC operating conditions.

1.8 Approach

The CFCC has developed the Separated Anode Experiment to decouple the mass transport and internal reforming reaction kinetics from the electrochemical reactions within a fuel cell. By allowing the experimenter to directly measure these critical aspects of anode operation, the SAE is able to provide unique insight into the anode performance with no need for electrochemical operation of the fuel cell. SAE based results have been previously published by Hecht et al., Storjohann et al. ,and Richards et al. (E. Hecht, 2005), (D. Storjohann, 2009),(A. Richards, 2010).

In addition to the SAE, morphological characterization experiments are conducted to identify physical characteristics of the two vastly different SOFC anode materials. The analysis of the physical morphology and composition of those samples is then directly correlated to the gas phase transport and reforming kinetics results from the SAE. This provides a straight forward evaluation of each sample's capability to perform the critical anode tasks of fuel reforming and subsequent transportation of that fuel to the reaction site. This evaluation is done independently of the anode's electrochemical operation, greatly simplifying the analysis and subsequent optimization of those characteristics.

2 BACKGROUND

SOFCs have been studied for multiple decades and are only now starting to reach marketability. SOFCs have been, and continue to be, limited by the available materials to support their operation. Common materials simply cannot survive long in the high temperature environment of the SOFC. Highly engineered and expensive materials like specialty ceramics and exotic alloys are commonly used to mitigate the effects of the operating environment, however even the best SOFC's still have limited operating lifetimes. High costs, short lifetimes associated with poor materials, as well as high temperature durability continue to be the most significant issues facing the SOFC technology and marketability.

2.1 Current SOFC materials

Current SOFCs are largely dependent on ceramic materials for critical components such as the cell support. Reliance on ceramics severely limits SOFC operation. Ceramics have poor thermal conductivity and are prone to fracture if heated or cooled too rapidly. The poor thermal characteristics of the SOFC coupled with its high operating temperature severely limits the electrical load following and rapid start up and shutdown capabilities of the device. The abilities to start up rapidly and adjust to dynamic electrical loads are important characteristics for electricity generation devices, especially in smaller systems such as transportation APUs and backup generators.

2.1.1 SOFC cell construction

SOFC cells have four main components; anode, cathode, electrolyte, and support. There are four main types of cell configurations that are currently used in SOFC design; electrolyte supported cells, cathode supported cells, anode supported cells, and metal supported cells. A diagram of the different constructions can be seen in Figure 2. The naming convention is straight forward. For example, in a cathode supported cell the cathode layer acts as both cathode and as the main mechanical support of the cell. Likewise for anode supported and electrolyte supported cells; the anode and the electrolyte, in addition to performing their electrochemical functions, act as mechanical support for the cell. Electrolyte supported cells are

generally the oldest architecture for SOFC construction. In order to minimize ohmic losses the electrolyte supported cells normally operate at temperatures of 1000C or greater. Electrode supported cells (anode or cathode supported) do not require a thick electrolyte layer for mechanical support. Consequently the electrolyte layer on those architectures can be substantially thinner. Thinner layers are more conductive and ohmic losses are decreased. The increase in conductivity of the electrolyte in electrode support cells allows them to be operated at lower temperatures (approximately 800 C). Popularity of the electrolyte supported cell has declined as the electrode supported architectures have become more popular (in particular anode supported); however, electrolyte supported cells are still used, a prime example being the SOFC cell used in the "Bloom Energy Server", from Bloom Energy.

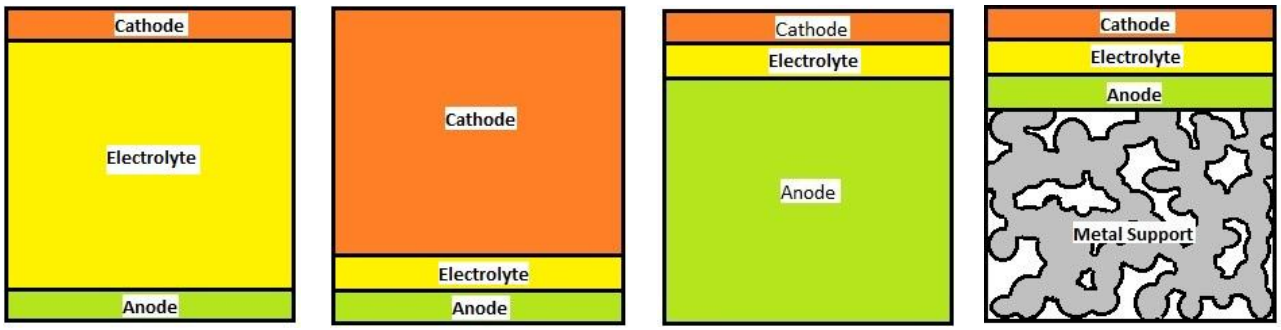

Figure 2- Schematic of the various SOFC cell architectures. Left to right; electrolyte supported cell, cathode supported cell, anode supported cell, and metal supported cell.

The newest type of cell construction for SOFC applications is the metal supported cell. In a metal supported cell a porous or laser drilled metal substrate is used to provide mechanical support for the cell. The simplest form of metal supported cells consist of the metal substrate with a conventional ceramic cell adhered to the surface of the metal. The use of a metal support for the SOFC has the ability to greatly increase the thermal cycling and startup capabilities of a SOFC. The metal substrate must be porous to allow fuel transport to the fuel cell that is adhered on the other surface. Typically the metal support is chemically inert and simply acts as a support for the cell. However, Yan et al. and Ishihara et al. have experimented with Ni based alloys to act as both support and anode (J.W. Jan, 2005),(T. Ishihara, 2008),(T. Ishihara, 2006). In this case the cell could be considered both anode and metal supported. Metal supports and metal supported cells are discussed in more detail in section 2.2.

Currently the most common SOFC style used is the anode supported cell. Anode supported cells are generally used more often than cathode supported cells for a few reasons:

- The polarization (activation) losses at the anode are less than at the cathode.
- The mobility of H_2 is higher than that of O_2. H_2 diffusion is less effected by the thicker electrode structure than O_2 would be.
- O_2 reduction kinetics tend to be slower than H_2 oxidation kinetics.
- A thicker porous anode structure increases the catalytic affective area (CAA) of the anode exposing more Ni catalyst for both electrochemical oxidation of H_2 and the reforming of HC fuels.
- The most commonly used cathode perovskites like $La_{0.5}Sr_{0.5}MnO_3$ (LSM) have a poor coefficient of thermal expansion (CTE) match to the most commonly used electrolyte material, YSZ. A poor CTE match can lead to mechanical stresses in the cell and result in cracking. Increasing the thickness of the cathode to provide mechanical support for the cell aggravates this issue.

2.1.2 SOFC anode functionality

Brandon and Brett list three main purposes that anode structures serve during SOFC operation:

- Transport of electrons to the current collector from the reaction site through an electronically conducting phase
- Acceptance of these electrons from a species absorbed on the electrode surface from the gas phase, to form ionic species.
- Transport of ions from the electrolyte through an ionically conducting phase (N.P Brandon, 2006).

In other words, the anode must be porous to allow the diffusion of fuel into and waste products out of the cell. The anode must be catalytically active to promote absorption of H_2 onto its surface. Finally the anode must be electronically and ionically conductive at the temperature of operation. In addition, if direct internal reforming will be used in the system, the anode must be catalytically active to promote the reforming of the HC fuel.

As discussed previously, the electrochemical reactions in the SOFC can only occur in a region where the O^{2-} ions, the H_2 gas, and electronically connected catalysts meet. This area is known as the triple phase boundary (TPB). Typically TPB is restricted to the anode-electrolyte interface because the relevant reactant species are bound to their respective surfaces. However, if the anode were a conductor of ions in addition to being a conductor of electrons, the reactant

ions would be free to transition from the electrolyte into the anode structure. This effectively makes the entire anode part of the TPB, drastically increasing the TPB surface area. Conductors of both ions and electrons are known as mixed conductors and are extremely attractive for SOFC anode applications.

2.1.3 Zirconia based anodes

Zirconia based anodes are currently the most commonly used SOFC anodes. The zirconia (ZrO_2) is typically stabilized with a transition metal oxide, most commonly yttria (Y_2O_3), leading to the name yttria stabilized zirconia (YSZ). While yttria is the most commonly used stabilizing compound, scandia (Sc_2O_3) can be used as well, which results in scandia stabilized zirconia (ScSZ). At SOFC operating temperature YSZ is chemically inert and a pure O^{2-} ion conductor, making it ideal for use as an SOFC electrolyte. In order to be used as an anode the YSZ material must be made catalytically active, electronically conductive, and permeable to gas transport. This is typically done by adding Ni to the ceramic. Ni is usually added in the form of NiO, which is then subsequently chemically reduced to Ni during start-up. The reduction of NiO adds the needed porosity for the anode to meet its mass transport requirements (typically 30% or greater (W.Z. Zhu, 2003)) while the remaining Ni adds the catalytic activity and electron conductivity. The YSZ ceramic structure provides mechanical stability for the layer and supports the Ni, helping to prevent Ni coarsening. The CTE of the zirconia based anodes can be adjusted by altering the particle size and ratios of the powders used, which allows the Ni-YSZ to be custom formulated to be compatible with numerous different supports or electrolytes. Ni-YSZ anodes have significantly improved sulfur contaminate tolerance when compared to low temperature catalysts like Pt; however, sulfur poisoning remains an issue and the deposition of sulphides can increase with reduced operation temperature (Y. Matsuzaki, 2000). Also, while the yttria or scandia support of the zirconia structure significantly reduces Ni coarsening, coarsening remains an issue with redox cycling of the cell, making long-term operation a concern.

Ni–YSZ anodes are commonly used in DIR applications because Ni is an excellent electrochemical catalyst and an acceptable reforming catalyst. While Ni is an effective reforming catalyst it is known to promote carbon coking if insufficient water is present for the SR reaction. Internal reforming concerns are discussed in greater detail in section 2.1.6.

2.1.4 Perovskite based anodes

Due to the limitations with the Ni-YSZ anodes, multiple other anode materials have been developed and tested. One of the leading alternatives to Ni-YSZ is the perovskite based anode. The key advantage of perovskite based anodes is that they promote HC reforming catalytic activity with low propensity for carbon formation. While reforming activity of most perovskites is modest compared to Ni-YSZ they can easily be modified though the addition of other reforming catalyst like Ru, which greatly improves their reforming capabilities. As perovskite anodes are Ni free they do not have Ni coarsening or sulfur poisoning issues.

Perovskites are poor O^{2-} ion conductors at low partial pressures of O_2 so they are frequently doped with elements such as La, Sr or Y to enhance their ion conductivity. Common perovskites used for SOFC anode applications are $La_{0.8}Sr_{0.2}Cr_{0.97}V_{0.03}O_3$ (LSVC), $La_{0.75}Sr_{0.25}Cr_{0.5}Ma_{0.5}O_3$ (LSCM), and $La_{0.8}Sr_{0.2}Mn_{0.8}O_3$ (LSSM), amongst many many others.

2.1.5 Ceria based anodes

Development of CeO_2 based anodes began because doped ceria is an excellent reforming catalyst for methane. Ceria is also attractive as it is a mixed electron and ion conductor in reducing environments without the need for doping. Unfortunately ceria becomes structurally unstable at high temperature due to lattice expansion caused by the chemical reduction of Ce^{+4} to Ce^{+3}. The structural instability of ceria can lead to cracking or even complete delamination of the anode layer. Ceria is often heavily doped with +3 cations like gadolinium (Gd^{3+}), samarium (Sm^{3+}), or yttrium (Y^{3+}) which replace a large amount of the Ce^{4+} cations in the structure, this adds significant stability to the structure at high operating temperatures.

The reforming performance of ceria can be improved by the addition of noble metal catalysts such as Pt, Rh, Pd, or Ru. It has also been shown that the addition of Ni to ceria can promote carbon-free reforming, likely due to the mixed conducting nature of the ceria layer, which allows for direct oxidation of methane on its surface with no need of an intermediate steps. However, the actual mechanism is debated.

2.1.6 Internal reforming considerations

In direct internal reforming systems the HC fuel is reformed into the necessary hydrogen fuel within the anode structure itself. With direct internal reforming the anode now supports two coupled but entirely different chemical reactions. A major issue with direct internal reforming systems is the fact that reforming reactions (SR, DR, WGS) have entirely different reaction

kinetics when compared to the electrochemical oxidation of hydrogen. Reforming rates of HC fuels tend to be much faster than the electrochemical oxidation rate within the anode. The rates of the reactions could be changed by altering the catalyst loading for each reaction; however, both the reforming and oxidation processes are typically catalyzed by the same catalyst making it impossible to customize the catalyst loading for each reaction. Fundamentally, the rate of the electrochemical reactions within a fuel cell is determined by the flow of electrons through its external circuit. Therefore the external electrical load on the fuel cell determines the rate at which the hydrogen fuel is consumed and product water is formed. The reforming reactions on the other hand have no external moderation control. The rate at which the reforming reactions take place is determined by the operating temperature, catalytic loading, and concentration levels of the reactants. As discussed in section 1.4.6, the amount of H_2O present during the reforming reaction is critical to the coking stability of the process. However, the amount of H_2O present in the anode structure is largely determined by the electrical load on the fuel cell. Unfortunately, simply humidifying the fuel and running with excessive amounts of water present to prevent coking in the anode would result in a lower reversible cell voltage via the Nernst equation (equation 2.1) which decreases cell efficiency (D. Morgensen, 2011). The Nernst equation describes the reversible cell voltage as a function of the activities (concentrations) of the products and the reactants of the electrochemical reaction, as shown below(R. O'Hayre, 2008).

$$E = E^0 - \frac{RT}{nF} \ln \frac{\prod a_{products}^{v_i}}{\prod a_{reacants}^{v_i}} \tag{2.1}$$

Where E^o is the standard electrode potential, R is the universal gas constant, T is the temperature, n the number of electrons transferred in the reaction, F is Faraday's constant, $a_{products}^{v_i}$ and $a_{reacants}^{v_i}$ are the chemical activities of the corresponding chemical products or reactants.

As can be seen, control of H_2O concentration is critical to DIR systems and extremely problematic. A more or less constant current density is required to sustain the reforming reactions without carbon deposition, which significantly limits the application flexibility of the system. A possible mitigation to the issues associated with single catalyst DIR systems is suggested by Rostrup-Nielsen et al. They have shown evidence that while the electrochemical and HC reforming reactions use the same catalyst, they do not in fact use the same reaction

sites. Rostrup-Nielsen et al. go on to say that selectively blocking specific reforming structures while leaving the electrochemical sites active may be a way to regulate the reforming reaction while maintaining electrochemical performance (J.R. Rostrup-Nielsen, 2006).

2.1.7 Inert barrier layers

Some researchers have proposed the use of inert barrier layers between the HC fuel and the active anode layer. The barrier layer retards the penetration of the HC fuel into the anode and helps moderate the reforming rate of the fuel. Lin et al. have shown that the current density a DIR cell requires for coke free operation can be substantially reduced with the addition of a thin inert barrier layer. The addition of this film significantly widened the low current density operating window. Lin et al. also noted a decrease in the high current density operating window due to concentration losses due to the barrier layer restricting fuel flow into the cell. It was also apparent the barrier layer cell had a lower reversible voltage, likely due to high concentrations of H_2O present in the anode. The barrier layer cell appeared to have increased ohmic polarization loses as well. This was likely due to poor electronic conductivity of the barrier layer (Y. Lin, 2006).

In Pillai et al. it was shown that the addition of CO_2 and/or air to the methane stream coupled with the use of an inert barrier layer increased coking stability. The addition of the barrier layer is also attributed to increase margin to anode cracking by slowing the endothermic reforming reaction, which can lead to cell cracking due to thermal stresses induced by localized cooling (M. Pillai, 2010).

While inert barrier layer addition may gain margin to coking at lower current densities, the addition of these layers will ultimately result in increased concentration losses at high current densities due to the decreased mass transport characteristics of the structure. Increased ohmic losses are also likely, due to additional electrical resistance between the anode and the current collector. Lower reversible potential due to H_2O trapping within the anode structure is also likely, especially at higher current densities.

2.1.8 Reforming specific catalyst layers

Another proposed idea to control the reforming reaction is to use a separate catalyst layer specifically for the reforming of the HC fuel. Similar to a barrier layer, the reforming specific catalyst layer is applied to the surface of the anode in between the anode and the fuel channel. Addition of the second catalyst allows for custom catalyst loading tailored to the reaction kinetics of the reforming reactions and allows for a different catalyst species to be used for reforming and

for the electrochemical reactions. The use of catalysts like Ru or Ir is especially attractive as they are known to be highly effective HC fuel reformers while not promoting carbon formation. The use of additional reforming specific catalyst layers is generally considered a form of indirect internal reforming (IIR).

Zhan and Barnett used a thin Ru-CeO_2 layer to demonstrate internal reforming of iso-octane with encouraging results (Z. Zhan, 2005). Klein et al. have demonstrated stable internal reforming of CH_4 using an Ir-CeO_2 catalyst layer applied to the surface of a standard Ni-YSZ anode. Unfortunately their cell suffered a premature death due to delamination, but the reforming results are encouraging (J.-M. Klein, 2009). Cheekatamarla et al. at NanoDynamics Energy, Inc. have used a proprietary catalyst applied to the surface of a Ni-YSZ anode to reform various hydrocarbon fuels (P.K. Cheekatamarla, 2008). Unfortunately NanoDynamics Energy filed for bankruptcy in 2009 so their development in this area has stopped(unknown, 2011).

There are disadvantages to using a separate catalyst layer as well. Zhan and Barnett noted increased concentration losses in the cell with the reforming catalyst layer due to mass transport reduction, similar to the behaviour noted with the inert barrier layer(Z. Zhan, 2005). Zhan and Barnett also note that the CeO_2 layer used is electronically insulating, which causes issues with current collection(Z. Zhan, 2005). Klein et al. placed Pt wires between the electrolyte layer and the anode to act as current collector for their cell to mitigate this issue(J.-M. Klein, 2008).

2.2 Metal supported cells

Metal supported SOFCs have many potential advantages over conventional ceramic supported SOFCs including; increased durability, greatly improved thermal cycling capability, increased redox tolerance, cheaper manufacturing, and improved stack level sealing options. Improved rapid thermal cycling, in particular, is a significant advantage; rapid response is often necessary in most small to medium sized systems. All these advantages have the potential to lead to decreased balance of plant complexity, longer system lifetime, and overall reduced system costs.

Metal supports for SOFCs have, to date, been of two general types, preformed metal sheets perforated by laser drilling to provide adequate mass transport or porous metal formed through powder metallurgy methods such as tape casting, pressing, or free-powder sintering. Both methods of support manufacture have advantages and disadvantages. Preformed sheets are generally flexible with the ability to be bent or twisted while porous metals are generally more brittle and tend to break or crack when bent. Porous metals tend to be thicker than preformed

supports as thicker sheets are needed for mechanical support. Due to the nature of laser drilling manufacturing, laser drilled supports have essentially zero tortuosity while porous samples will have significantly higher tortuosity. The lack of tortuosity of a laser drilled sample promotes higher mass transport for given porosity level in the laser drilled supports (N. Oishi, 2010). This implies that laser drilled supports will generally require lower porosity to support the needed mass transport within an operational cell. Preformed sheets have regular dense surfaces which promote easier coverage for anode and electrolyte depositions which has the potential to lead to thinner films and higher conductivity. Laser drilled samples will also have less exposed surface area, allowing for greater resistance to oxidation and potentially longer lifetimes at higher temperatures for reasons that will be discussed in section 2.2.2. Greater surface area may, however, be desirable if the support is also acting as anode due to increased reaction sites at the TPB. Porous metals have potential advantages in internal reforming applications where the intrinsic tortuosity of the support may help prevent excessive water loss, promoting a more complete and coking free SR reaction. Laser drilling also has a significant disadvantage due to its high cost for mass production.

The manufacture of a metal-supported SOFC starts with the choice of support material. Multiple metals have been used to support SOFCs including; Ni, NiFe, NiCrAlY, Hastelloy-X, 300 series austenitic stainless steel, 400 series ferritic stainless steel, Crofer, and ITM . In order to ensure long cell life, especially in high-cycle applications, the coefficient of thermal expansion (CTE) of the metal support should be matched to the anode and electrolyte layers. In addition the metal supports should have a high resistance to oxidation in the SOFC operating environment and be relatively low-cost. A summary table of proposed metal supports can be seen in Table 1. The metals currently used as SOFC supports can be classified into two general categories, nickel (Ni) based metals and iron (Fe) based metals.

2.2.1 Nickel based metal supports

Multiple groups have manufactured functional cells using a plain porous Ni substrate. Hwang et al. manufactured Ni-YSZ/LSGM/LSCF cells on a porous Ni substrate (C. Hwang, 2008). Cho et al. used porous Ni to support a conventional Ni-YSZ/YSZ cell (H.J. Cho, 2009). Metal supports are not always inert bystanders to the electrochemical reactions taking place in the fuel. Ni supports, in particular, can perform both as anode and support. In Mineshige et al, Ni supported small, tubular cells were built where the porous Ni support acted both as anode and support (A. Mineshige, 2006).

Pure Ni supports have significant limitations making them unlikely to be adopted as a long-term metal support solution for SOFCs. Referring to Table 1 it can be seen that the coefficient of thermal expansion (CTE) of Ni is significantly higher than that of commonly used electrolytes like YSZ, CGO and LSGM, which have CTE values of 10-12 ppm/K. In addition to the CTE mismatch, Ni metal is susceptible to carbon coking in an internal reforming environment and is highly susceptible to sulfur damage as discussed previously. Ni is also a high-cost metal.

In order to overcome some of the challenges faced by pure Ni supports, Ni-Fe alloys have been used to support SOFCs. Referring to Table 1, the addition of Fe to the Ni changes the CTE to be a better match with the commonly used electrolytes. The addition of Fe also decreases the cost of the support. Ishihara et al. have constructed numerous IT-SOFC cells using a NiFe alloy acting as both support and anode. They note that the addition of Fe to the Ni substrate lowers the anodic over potential with a minimum seen at 10%wt Fe (T. Ishihara, 2008)(T. Ishihara, 2006) . Further investigation into the NiFe mixture has been conducted by Zhu et al. They suggest a 1:1 weight ratio has the best possible CTE match to the commonly used ceramic electrolytes(J. H. Zhu, 2007). While the addition of Fe to Ni lowers the cost and improves the CTE issues, susceptibility to sulfur and coking remain.

Porous Hastelloy-X plates from the Mott Corporation have been used by the Institute for Fuel Cell Innovation in Vancouver BC as a support for SOFC cells with a Ni-SDC anode and SDC electrolyte(R. Hui, 2009)(Z. Wang, 2008). Hastelloy-X is a commonly used alloy for high temperature applications in industry and has excellent oxidation resistance characteristics. Hastelloy-X is a complex alloy consisting of approximately 47% Ni, 22% Cr, 18% Fe, 9% Mo, 1.5% Co, 0.6% W with trace amounts of C, Mn, Si and B. Referring to Table 1, it can be seen that Hastelloy-X has a poor CTE match to commonly used electrolytes. It is also significantly more expensive than both pure Ni and 1:1 Ni Fe. For these reasons, Hastelloy-X does not seem to be a viable support for mass adoption.

2.2.2 Iron based metal supports

Numerous studies have been conducted on Fe based metals for use as support for SOFC. Both 300 series austenitic stainless steels and 400 series ferritic stainless steels are attractive options for mass-produced supports because they are inexpensive, and the technology associated with their production and forming is well understood. Molin et al. performed an evaluation of 316L porous stainless steel. They showed significant rates of oxidation, even while in a H_2 rich reducing environment. Molin et al. also noted that austenitic steels such as 316L form non-conductive Fe-

Cr oxides at temperatures typical for SOFC operation (S. Molin, 2009) . Formations of non-conductive oxides increase the electrical resistance of the support making it impractical for use as a current collector in an SOFC. Referring to Table 1 there is also a significant CTE mismatch with austenitic steel and common electrolytes. For these reasons Molin et al. concluded that 300 series stainless steels are a poor choice for SOFC supports (S. Molin, 2009).

Due to the limitations of the other supports, ferritic stainless steels are generally accepted as the alloy of choice for metal-support SOFCs (Tucker, 2010). Ferritic stainless steels (400 series stainless steels) have many advantages over other supports. 400 series alloys are cheap and their manufacturing process is straightforward and well understood by industry. Referring to Table 1, it can be seen that 400 series SS also has an excellent CTE match to the commonly used electrolytes. Ferritic SS have excellent oxidation resistance and are regularly used for high temperature applications like automotive exhausts and refinery applications. They typically contain between 10.5wt% and 26wt% Cr. The high Cr content in the metal is critical as the formation of a chromia scale is necessary to protect against further oxidation of the substrate. Chromia scale is also conductive, which maintains the electrical conductivity of the support and allows it to operate as a good current collector (S. Molin, 2010).

Molin et al. performed an evaluation of porous 430L Stainless steel as a potential SOFC support. They noted higher than expected oxidation rates in the porous sample when compared to dense 430L oxidation rates (S. Molin, 2008). They also noted that the formation of both Fe_2O_3 and Cr_2O_3 scale was present in the porous sample when compared to the dense sample, in which only Cr_2O_3 scale was present. They concluded that despite the 16-18wt% Cr in the 430L sample, the amount of Cr present was insufficient to form a continuous chromia scale due to the increased surface area exposure of a porous sample. The lack of a continuous chromia scale in the sample lead to the formation of a non-conductive Fe_2O_3, which increased the sample's ASR.

Table 1- Summary of proposed SOFC support metals

Alloy	Structure	CTE ppm/K	Oxidation Resistance	Alloying Elements %				Source
				Cr	Ni	Fe	Other	
Ni based								
Ni	Austenitic	16.5	Very Poor	-	100	-		(Tucker, 2010)
Ni-Fe (1:1)	Austenitic	13.7	Very Poor	-	50	50		(Tucker, 2010)
Ni 625	Austenitic	9-10	Good	19.4	Balance	1.9	Si=0.37,Mo=11.2, Mn=0.16	(A. Bautista, 2008)
Ni20Cr	Austenitic	17.3	Fair	19.05	Balance	0.1	Si=0.72,O=0.04 N=0.04,Mn=0.21	(A. Bautista, 2008)
PI600	Austenitic	13.3	Very Good	15.56	Balance	9.11	Si=0.84,Mn=0.05	(S. Molin, 2010)
Hayes 230	Austenitic	14.8-15.7	Good	22	Balance	< 3.0	W=14.0,Co = 5.0 Mo=2,Mn=0.5	(S. Molin, 2008),(Haynes International, 2007)
Hastelloy-X	Austenitic	15.5-16	Very Good	22	Balance	18	Co =1.5,W=0.6, C= 0.10, B<0.008,Si<1.0	(Tucker, 2010),(Haynes International, 1997)
Fe Based								
300 SS	Austenitic	18-20	Poor	>10.5	Var	Balance	Var	(Tucker, 2010)
317L SS	Austenitic	19	Poor	18.27	11.87	Balance	Si=0.85,Mo=3.04, Mn=0.12-	(S. Molin, 2010)
400 SS	Ferritic	10-12	Good	>10.5	Var	Balance	Var	(Tucker, 2010)
430L SS	Ferritic	11.5	Good	16.0-18.0	-	Balance	Si<1.0, Mo<0.5,Mn<1.0-	(S. Molin, 2008),(A. Bautista, 2008),(L. Rose, 2009)
ITM	Ferritic	10-12	Excellent	26	-	Balance	Ti, Y2O3	(T. Franco, 2007)
Fe22CR	Ferritic	11.5-12.5	Very Good	22.3	-	Balance	Si=0.16, Mn=0.48 Ti=0.31,La=0.34	(A. Bautista, 2008),
Crofer22APU	Ferritic	11.5-12.5	Very Good	20.0-24.0	-	Balance	Mn<0.8,C<0.12, Cu <0.5	(I. Antepara, 2010),(I. Antepara, 2005),(S. Fontana, 2007),(ThyssenKrupp VDM, 2005)
E-brite	Ferritic	11.5-12.5	Very Good	26.0-27.5	<0.5	Balance	Mo<1.5, <0.4 C<0.01, Cu<0.5	(ATI Allegheny Ludlum, 2007) ,(S. Molin, 2008)

Materials used as interconnect materials in SOFCs tend to be strong candidates for cell supports. Interconnect materials in SOFC stacks join adjacent cells by providing electrical connection between cells and by providing fuel and exhaust ducting. The environment seen by the interconnect material is essentially the same environment that is seen by SOFC supports. In addition to the similarities in the environment, the physical requirements for the interconnect materials and support materials are similar in that both are desired to have good CTE match to common electrolytes, to be highly conductive, to have high oxidation resistance, and to be inexpensive. Given the similarities in the requirements, successful interconnect materials should also be satisfactory candidates for metallic supports. A recent study by Ikerlan-Energia investigated a leading metallic interconnect material, Crofer22APU for use as porous metal support of SOFCs. In the study Crofer powder was pressed and sintered to three different porosity levels. The oxidation rate of each porous sample was measured using thermogravimetric measurements from 600C to 800C in a humidified hydrogen environment consistent with conditions present within a SOFC. It was found that all samples oxidized with the lowest porosity samples showing the lowest rate of oxidation. The increased resistance to oxidation in the low porosity samples is attributed to the lower surface area present in the samples. This study concludes that even Crofer, which is a leading metallic interconnect for SOFC applications is currently incapable of meeting the lifetime demands for a porous metal support(I. Antepara, 2010).

Plansee SE has developed a porous metal support based on its popular ITM alloy. ITM is an oxide dispersive strengthen (ODS) ferritic FeCr alloy Fe-26Cr-(Mo, Ti, Y_2O_3). Dense versions of the ITM alloy are commonly used as interconnect material for high temperature SOFC stacks such as the emerging "Energy Server" from Bloom Energy (Plansee SE, 2010). The porous ITM is manufactured using powder metallurgy (PM) techniques, which gives the support a high porosity to facilitate the transport of fuel. In the PM manufacturing route used by Plansee SE, the material does not reach its melting point, and hence no significant evaporation and segregation processes can occur. This leads to a more homogenous elemental distribution in the alloy and enables the formation of well-adherent protective oxide scales during the cell operation (T. Franco, 2007). A recent study by Franco et al. compared the porous ITM support to ingot metallurgy based Fe22Cr alloy (similar to Crofer). Thermogravimetric results of this study can be seen in Figure 3.

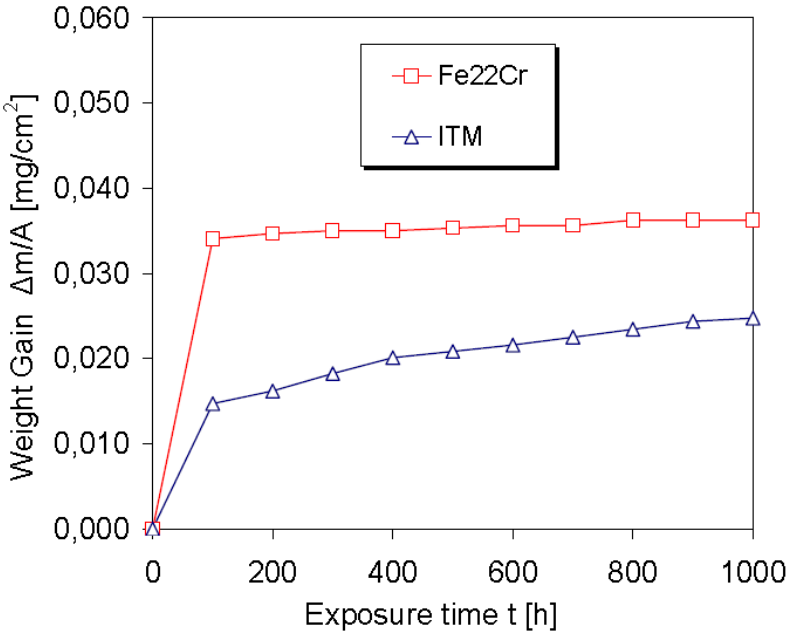

Figure 3- Oxide growth behavior of Plansee ITM compared to ingot based Fe22Cr substrate. Figure taken from Franco et al. (T. Franco, 2009)

The TGA results show that the ITM alloy had a significantly lower initial weight gain (within the first 100 hours) and that after 1000 hours the ITM alloy had only experienced approximately 70% weight gain seen by the Fe22Cr alloy(T. Franco, 2009). It is implied from this result that the ITM alloy is more resistant to oxidation than the Fe22Cr sample. It is important note, however, that nearly all of the weight gain experienced by the Fe22Cr alloy was within the first 100 hrs, while the initial oxidation of the ITM sample only constituted 60% of its total 1000 hour weight gain suggesting that the ITM sample may actually have a higher rate of oxidation for longer term operation. By extrapolating the data provided by Franco et al. (Figure 3) and assuming stable long-term oxidation rates, it can be seen that the weight gain of the ITM sample may in fact surpass that of the Fe22Cr sample after approximately 2000 hours in the TGA. It is hypothesized by Molin et al. that a high initial mass gain followed by slow mass gain can be beneficial if one takes into account the possibility of pre-oxidation of alloy prior to deposition of the ceramic layers(S. Molin, 2010). No XRD, EDX, or ASR data on the ITM or Fe22Cr alloys is reported by Franco et al. So it is impossible to determine if the weight gain in either sample was due solely to growth of the protective and conductive Cr_2O_3 scale or due to growth of both a Cr_2O_3 and Fe_2O_3 which would be detrimental to the life of the supports.

Molin et al. have noted in various studies of porous metals that oxidation rates in the porous samples are significantly higher than dense versions of the same alloys (S. Molin, 2008),(S. Molin, 2010),(S.

Molin, 2009). These findings are similar to the findings of Antepara et al. and Bautista et al. (I. Antepara, 2010),(I. Antepara, 2005),(A. Bautista, 2008) . The studies mentioned have included some of the most advanced alloys for SOFC applications; however, none have shown an alloy to be capable of long-term operation at 800C. Tucker notes that there is ample evidence that appropriate coatings, treatments, or alloy modifications can reduce oxidation rate and increase scale adhesion for dense interconnect materials. Exploring similar options for porous supports should be a focus for further research (Tucker, 2010).

2.3 Operation temperature

It is generally known that higher operating temperatures lead to higher rates of oxidation of metallic components in SOFCs. It is also known that lowering the operating temperature lowers the stresses and strains on components that are caused by CTE mismatch and thermal cycling. As discussed in section 1.2, lower operating temperatures lead to decreased conductivity of ceramic electrolytes and decreased catalytic activity for internal reforming and hydrogen oxidation reactions. This leads to efficiency losses in the system. Many metal supported SOFC researchers and manufactures have begun to focus on lower temperature metal supported SOFC systems that operate between approximately 400C – 800C, these systems are often referred to as intermediate temperature solid oxide fuel cells (IT-SOFC). Lowering the operating temperature of the system allows for use of more common place alloys as support. Ceres Power Ltd. for example is arguably the leading metal supported SOFC manufacture in the world. Their systems have a reported operating temperature of approximately 575C (N.P. Brandon, 2004). Due to their lower operating temperature, Ceres power is able to use common 400 series Stainless steel foil as their support. In order to achieve this lower operating temperature Ceres Power has had to pursue alternative electrode and electrolyte materials. It is also important to note that operating temperatures lower than approximately 625C are generally considered too cool for stable internal reforming systems, requiring use of an external reforming system, which increases system complexity (Tucker, 2010). Lower operating temperatures are currently the only real option for long term reliability of metal supported SOFC systems; however, there are significant tradeoffs associated with electrical conductivity and catalytic activity.

2.4 Ceramic cell components for metal supported cells

Compatibility of metal support and anode/electrolyte is critical for long term stability and reliability of the cell. In order to avoid material compatibility issues like CTE mismatch and co sintering

issues, typical cell designs use catalyst doped porous anode materials based on the same general bulk material of the dense electrolyte. Metal support and electrolyte/anode CTE must match within an acceptable margin to prevent stress related failures. As operating temperature and thermal cycling requirements decrease, the need for CTE match is also decreased. Also, as system operating temperature is decreased, electrolyte resistance increases, leading to increased ohmic losses in the system. The metal support must be capable of long term operation at a temperature necessary for the electrolyte to conduct ions effectively; while the electrolyte must be able to conduct ions effectively at a low enough temperature for the metal support to survive long term. Currently the only commercially viable metal supported SOFCs operate at temperatures that are generally insufficient to sustain internal reforming and require higher conductive electrolytes and more electrochemically active anodes than the standard YSZ and Ni-YSZ materials.

2.4.1 Zirconia electrolytes and anodes

Yittria stabilized zirconia (YSZ) is the most common electrolyte used in SOFC systems. It has many advantages over other electrolyte options. YSZ is a mature, well-established material with a proven track record of high performance and longevity. It is an inexpensive material that is widely used in industrial applications lending to long-term price stability and availability (Tucker, 2010). At operating temperature YSZ is an excellent ion conductor while maintaining essentially zero electronic conductivity. YSZ is also capable of stable operation at temperatures necessary to support internal reforming of HC fuels. The key disadvantage of YSZ is its requirement of high system operation temperature for adequate ion conduction. Operation temperature necessary for ion conduction can be mitigated somewhat by thinning the electrolyte layer; however, that can lead to increased electron leakage due to poor film coverage. The lower bound for YSZ based system operation is not likely to be less than 700C with most current systems operating at 800C which is too high for sustained reliable operation of any current porous metal support. Ni-YSZ is the most commonly used anode material with the YSZ electrolyte. The German Aerospace Center (DLR) and their industry collaborator Plansee SE have pioneered the use of Ni –YSZ/ YSZ based cells supported by porous ITM alloy manufactured by Plansee, although they are still in the development stage. (P. Szabo, 2009),(T. Franco, 2007),(T. Franco, 2009) .

2.4.2 Ceria based electrolytes and anodes

Gadolinium-doped ceria (CGO) and samaria-doped ceria (SDC) are popular electrolytes for IT-SOFC applications with operating temperatures below 600C. Ceria based electrolytes benefit from

high ion conductivity allowing for their use at significantly lower temperatures than the standard YSZ based systems. Lowering the system temperature enables the use of commonly produced 400 series stainless steel alloys as cell support. Ceres Power ltd has effectively demonstrated CGO based cells supported by a fairly standard Ti – Nb stabilized stainless steel alloy with approximately 17% Cr content (N.P. Brandon, 2004) . Ceria based electrolytes do have the distinct disadvantage of not being able to operate at higher temperatures. At high temperatures the Ce^{4+} ions present in the film are reduced to Ce^{3+} ions in the reducing anode environment. The reduction of Ce ions within the film results in increased electronic conductivity which leads to an internal short of the fuel cell, decreasing system efficiency. It has been shown by Steele that Ce ion reduction in CGO is minimized at temperatures below 600C (Steele, 2000). Huang et al. demonstrated similar results for SDC (Q-A. Huang, 2009). The work of Steele and Huang et al. has therefore defined the upper bound for operation temperature of ceria electrolytes to be 600C. This is generally believed to be too low to support internal reforming of HC fuels, which means ceria based systems will be dependent on external reforming systems or pure hydrogen as fuel. Brandon et al. do point out however that 600C is a high enough temperature to support the WGS reaction in the anode (N.P. Brandon, 2004). Typical anodes used with metal supported ceria based cells are either porous Ni-CGO or Ni-SDC.

2.4.3 LSGM electrolytes

Strontium and magnesium-doped lanthanum gallate (LSGM) was initially developed at Oita University by Ishihara et al. in 1994 (T. Ishihara, 1994). LSGM is a perovskite based ceramic and is an excellent ion conductor which enables SOFC operation at low temperatures. Ishihara et al. have reported successful metal supported LSGM based cell operation from 400C – 700C (T. Ishihara, 2006). LSGM has the disadvantage of being reactive. Tucker et al. have shown LSM based materials to react with Cr vapor and Cr_2O_3 which significantly limits its potential for use with stainless steel based supports (M.C. Tucker, 2006). LSGM has also been shown to react with Ni, making direct contact of the LSGM and Ni doped anode materials or Ni containing support materials problematic. To mitigate the reactivity issues with LSGM Ishihara et al. have used thin SDC layers to chemically isolate the LSGM from Ni containing components (J.W. Jan, 2005) . Use of these layers ads additional ohmic impedances to the cell and as noted earlier the stability of SDC layers at temperatures greater than 600C is questionable. Metal supported LSGM based cells prepared by Ishihara et al. have demonstrated impressive power densities for IT-SOFC operation; however, the

long term reliability of cells is questionable and is as of yet untested. Ishihara et al. typically use a Ni-Fe bimetallic support as the anode for their LSGM cells (T. Ishihara, 2006).

2.5 Processing issues associated with metal supported cells

In addition to the many operation and longevity issues associated metal supports, there are multiple issues associated with the manufacturing of the cells. Typical ceramic parts are sintered in environments that would destroy metals by melting or through oxidation. Great care must be taken in the manufacturing process and Tucker has noted that similar materials can produce highly contrasting results when different manufacturing techniques are used. Processing considerations play a key role in effective cell design (Tucker, 2010). Tucker also notes that any cell processing above 900C should be done in a reducing environment or in high vacuum to prevent the substrate from oxidizing. Unfortunately NiO is reduced in that environment, which can lead to significant Ni coarsening. This lowers the catalyst loading at the TPB, which in turn leads to decreased electrochemical activity of the anode (Tucker, 2010).

Another critical issue associated with metal supported cells is when Ni containing anodes are in direct contact with steel supports. Inter diffusion of the Ni, Cr and Fe atoms can occur. Inter diffusion can occur during operation of the SOFC at any temperature but is greatly aggravated during high temperature processing steps. Ni migration into the steel support can cause the support to convert to the austenitic phase which greatly affects the CTE of the support. Cr/Fe migration into the anode leads to the formation of insulating oxides which leads to catalyst deactivation and conductivity decreases (Tucker, 2010). Multiple studies have investigated the addition of diffusion barrier layers (DBL) to mitigate the inter diffusion of the Ni, Cr, and Fe. Franco et al. have reported significant success in using perovskite based DBLs placed between porous ITM support and Ni-YSZ anode (T. Franco, 2007).

3 EXPERIMENTAL METHOD

Understanding the mass transport and internal reforming characteristics of the SOFC anodes is critical to the long term viability of the technology. While ceramic based cells have been studied extensively in this area, metal supported cells have not received the same treatment. In this work, a state of the art Ni-YSZ anode (CoorsTek reaction sintered Ni-YSZ) will be compared to a leading next generation porous support (Plansee SE ITM) in regards to mass transport and reforming capabilities. Analysis techniques used are liquid picnometry (Archimedes' Method) using distilled water, mercury porosimetry, SEM image analysis, and Separated Anode Experiment (SAE) to compare gas transport and internal reforming performance of the anodes.

3.1 Sample fabrication

3.1.1 CoorsTek reaction-sintered Ni-YSZ Anode

The standard for comparison used in this study is a Ni-YSZ anode that was developed and patented by CoorsTek Inc (W.G.Coors, 2007). The preparation of the CoorsTek reaction sintered anode is detailed in Storjohann et al. (D. Storjohann, 2009). Anode preparation begins with combining and ball milling 92 mol% monoclinic zirconia powder with 8 mol% yttria powder (Advanced Material Resources, Toronto, Ontario). The yttria-zirconia powder is dried, screened, and then blended with 65 wt% nickel oxide (OMG, Westlake, OH). The anode powder is then mixed with a binder specific to the final forming process. In the case of this study, the anode is dry pressed. The slurry is then spray-dried into a rotary atomizer. The NiO powders used for the reaction sintered process have a particle size of 10 μm. No pore former is needed for this process as the reduction of NiO into Ni within the sample during startup will provide adequate porosity. The powders used for Ni-YSZ anode formation at the Colorado Fuel Cell Center (CFCC) are provided by CoorsTek, Inc.

At the CFCC, 10g of powder is pressed into discs using a uni-axial press (Carver AutoFour30) loaded to 53.4 kN and held for 10 seconds. The green discs are then placed onto YSZ-Al_2O_3 porous setter plates (Selee Ceramics) and sintered in ambient pressure air at 1400C for four hours(D. Storjohann, 2009). After sintering, the anode measures 4.43cm in diameter and is 1.45 mm thick (Richards, 2010). The sintered anode disc is then shaped to the desired format using a diamond cutting wheel and surface grinding plates. For SAE experiments, the anode edge is sealed using alumina paste (Cotronics 989FS) to prevent gas leakage from the sides of the sample. The CoorsTek

sample used in this study was prepared by Amy Richards at The Colorado School of Mines, Colorado Fuel Cell Center.

3.1.2 Plansee porous ITM support

Plansee SE has developed a porous metal support based on its popular ITM alloy. The ITM is an oxide dispersive strengthened (ODS) ferritic FeCr alloy, Fe-26Cr-(Mo, Ti, Y_2O_3). The porous ITM is manufactured using powder metallurgy (PM) techniques, which gives the support a high porosity to facilitate the transport of fuel. In the PM manufacturing route used by Plansee, the material does not reach its melting point, and hence no significant evaporation and segregation processes can occur. This leads to a more homogenous elemental distribution in the alloy and enables the formation of well adhered protective oxide scales during the cell operation (T. Franco, 2007). The porous ITM substrate was delivered to the CFCC in 1mm thick plate form. A standard metal cutting band saw was used to rough cut the sample and a surface grinding wheel was used for final shaping of the sample to the desired size. Alumina paste (Cotronics 989FS) was used to seal the edges of the ITM sample for SAE testing. No AFL was present on the ITM sample analyzed in this study.

3.2 Sample characterization

As detailed in section 2.1.6, internal reforming anodes and supports must have multiple characteristics in order to perform well in an operational SOFC environment. Two of the most import characteristics are the mass transport and internal reforming capabilities of those structures. Multiple properties of the anode/support materials influence their transport and internal reforming characteristics including porosity, pore size, particle size, reforming catalytic activity, reforming catalytic surface area, and structure tortuosity. In addition to the SAE, several other characterization techniques are used to gain a more complete understanding of the sample structures. Scanning electron microscopy (SEM) is used to understand the surface and cross sectional morphology of the samples. Porosity measurements using Archimedes method (distilled water) and mercury porosimetry are used to measure sample porosity (ϕ), mean particle diameter (d_p), and mean pore size (r_p). These characteristics are then used in computational model to estimate sample tortuosity (τ_p).

3.2.1 Scanning electron microscopy of anode and support

Cross-sectional and surface SEM images are captured using an FEI Quanta 600i environmental SEM. Using the SEM qualitative and quantitative comparisons of the samples can be made using images of various magnifications. Image comparisons between samples can provide a general understanding of how the surface and cross-sectional structures compare. With high magnification images, particle size and pore size of each sample can be estimated

3.2.2 Porosimetry measurements

For this experiment, two different porosimetry measurements were used, Archimedes' method and mercury porosimetry. Archimedes method of this study used DI water as a fluid. Three separate samples of each anode were each weighed and then placed in boiling DI water for three hours. The samples then soaked for an additional two hours. After soaking, the samples were removed and weighed. Samples were then suspended in DI water and weighted for a third time. Sample porosity can then be calculated using the equation below (equation 3.1).

$$v_{open}^{\%} = \frac{m_{sat} - m_{dry}}{m_{sat} - m_{suspended}} \tag{3.1}$$

Where m_{sat} is the saturated mass of the sample, m_{dry} is the mass of the dry sample, and $m_{suspended}$ is the mass of the sample when suspended in water.

Mercury porosimetry measurements for this experiment were conducted by a third party materials characterization company, Micromeritics in Norcross Georgia, USA. Micromeritics use an AutoPore IV 9500 series mercury porosimetry apparatus. Mercury porosity works on the principle that the pressure required to intrude mercury (Hg) into the sample's pores is inversely proportional to the size of the pore. By measuring the volume of Hg that penetrates into the sample at multiple different pressures, the pore size distribution and porosity volume percentage of the sample can be measured (Micromeritics Instrument Corporation, 2010).

3.3 The separated anode experiment

The Separated Anode Experiment has been developed by the CFCC to provide a means for decoupling the internal anode reforming processes from the internal anode electrochemical

processes. The SAE was originally outlined and developed by Hecht et al. (E. Hecht, 2005),(Hecht, 2005). The SAE has since been used by Daggett, Gupta, and Richards (Daggett, 2008), (G.K. Gupta, 2006),(Gupta, 2007), (Richards, 2010),(A. Richards, 2010), (A. Richards, 2011).

The SAE setup used for this experiment was built by Amy Richards at the CFCC and contains many modifications and improvements from the setup that was originally reported by Hecht et al. Chemically inert ceramic manifolds and tubing are now used within the hot zone of the experiment, greatly decreasing the possibility of contamination. An improved sealing method using glass filter paper and mica sheets has significantly improved the gas leakage during the experiment. Improved start-up procedures have been implemented to prevent anode damage during start up. The mass spectrometer that was originally used has been replaced with a gas chromatograph, greatly improving the repeatability of the gas composition measurements. The experiment has also been modified so that the gas pressures in the fuel gas manifold and electrolyte gas manifold can be monitored and balanced using a water column, better representing the actual anode environment seen within an operational SOFC.

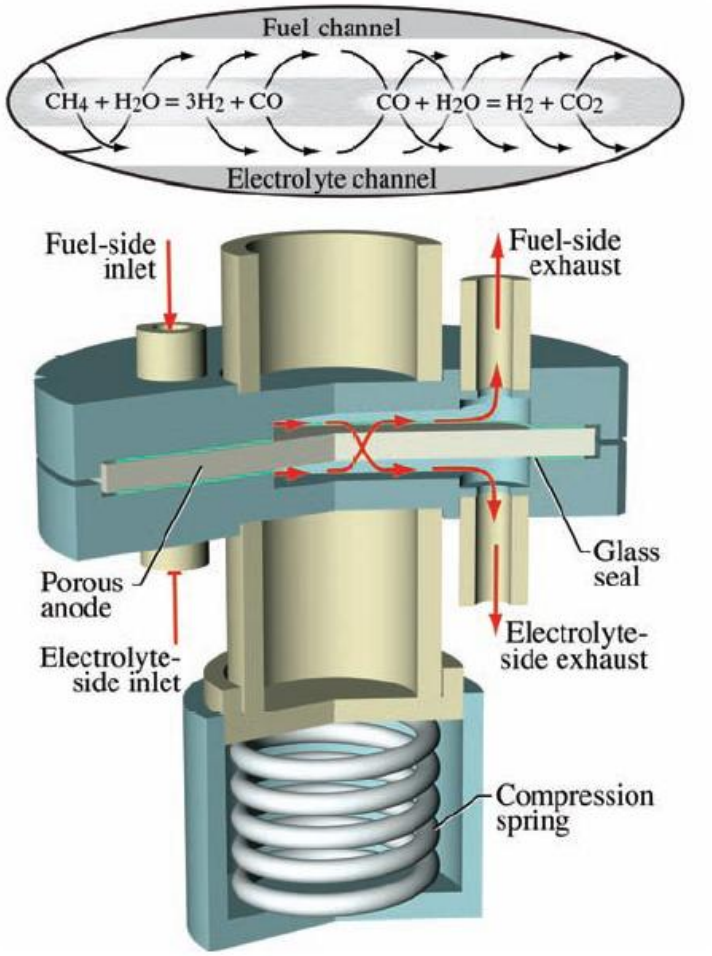

Figure 4- Cutaway illustration of the Separated Anode Experiment setup. Diagram from Hecht et al. (E. Hecht, 2005).

3.3.1 SAE design

An illustration of the SAE setup is shown in Figure 4. The anode sample is placed between the two ceramic gas manifolds. 0.6 mm thick mica paper seals (McMaster-Carr) are placed between two borosilicate glass filter paper seals (Fisher Scientific). A mica/glass seal is placed on each side of the sample between the sample and ceramic manifold as seen in Figure 5. This sealing method is based on the method used by Chou et al. (Y.-S. Chou, 2002).

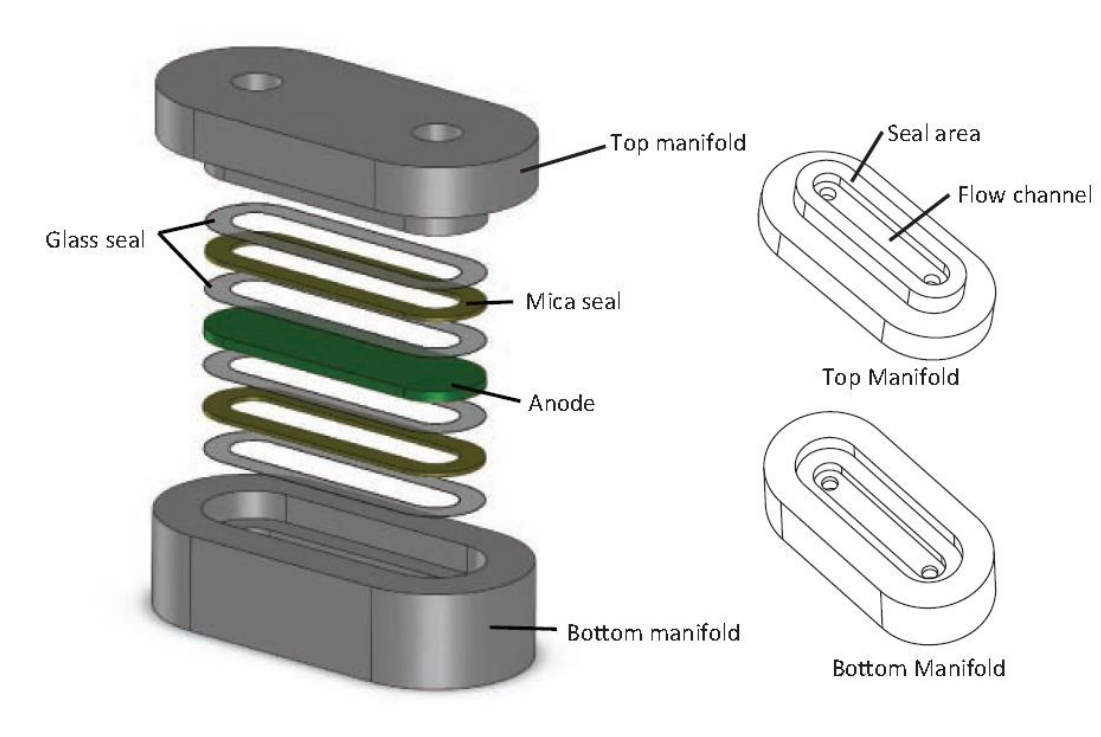

Figure 5- Exploded view of SAE manifold assembly and anode sealing process. Diagram taken from(Richards, 2010)

The manifold and sample assembly is then placed into a furnace and compressed for sealing. Gas connections are then coupled to the manifolds using compressive Swagelok fittings. The assembly is then heated to SOFC operating temperature (800C). As the sample is heated, the glass paper seals will melt and penetrate into the surfaces of the mica, ceramic manifold, and the sample, creating a better and tighter seal. The SAE has the ability to operate at various temperatures. However, for the extent of this study, all experiments are conducted at 800C.

Referring to Figure 4, it can be seen that each manifold has an inlet tube and an exhaust tube. The top manifold is the fuel manifold. During reforming testing, the fuel manifold is fed with a gas composition consistent with SOFC fuel mixtures. The bottom manifold is the electrolyte manifold. During reforming testing, it is fed with a gas composition that would be present at the TPB of the cell. The presence of the fuel mixture on the fuel side and electrolyte gases on the electrolyte side allows for the simulation of the internal reforming anode environment with no need for electrochemical reactions to occur. Thermocouples are placed at the anode surface to monitor sample temperature. The gas flows are controlled using mass flow controllers (MFC) (Alicat Scientific) accessed through a custom LabVIEW interface running on a standard desktop PC.

The gases present on the fuel side and the gases present on the electrolyte side cross diffuse through the anode structure in opposite directions. While diffusing through the anode, the gases are free to react with each other in reforming reactions to produce hydrogen, carbon monoxide, and other reforming product gases. The excess reactants and products from these reactions then diffuse to either the fuel or the electrolyte manifold channels and exit through the corresponding exhaust. The exhaust gas compositions are measured using a gas chromatograph (GC) (Agilent MicroGC 3000). Prior to reaching the GC, water vapour is condensed out of the exhaust streams using a counter flow dryer (Perma Pure MD Series). The use of the counter flow dryer prevents the build up of water within the stainless steel tubing of the experiment.

The exit gas compositions are directly related to the mass transport and internal reforming characteristics of the anode sample and can therefore be used to predict the performance of the anode in an operational SOFC. There is no electrolyte or cathode present in the experiment. As such there is a complete decoupling of the electrochemical processes from the reforming and gas transport processes present in the anode. The design of the SAE allows the experimenter to directly measure the anode's mass transport and internal reforming capabilities without having to consider the electrochemical interactions.

3.3.2 Start up and maintenance procedure

The CoorsTek anode is placed into the experiment in a dense green state, meaning the NiO used in the manufacture of the anode has not yet been chemically reduced to Ni. When the NiO is reduced the porosity of the anode is formed and Ni becomes chemically active and is available to act as a reforming catalyst. A critical aspect of the start up procedure is this reduction process. By exposing the anode to a reducing environment during the heating period, NiO is reduced to Ni. Care must be taken during the reducing process and the heating of the sample. If the sample is heated too quickly or if it is exposed to too aggressive of a reducing environment in the early stages of the start up process, excessive stresses on the ceramic structure can occur leading to sample fracture(Richards, 2010). The CoorsTek sample was heated from room temperature to 800C over a period of 800 minutes. During the heating period, forming gas (96.5% N_2 + 3.5%H_2) is flowed over the sample at a rate of 50 sccm in each channel. Once the sample has reached 800C the gas composition and flow is changed to 67% H_2 and 33% N_2 at a flow rate of 75 sccm in each channel. The sample is held in this environment for 48 hours to ensure complete reduction of the NiO has occurred. Once the sample has been reduced the CO_2 transport and reforming tests are performed. In between tests, the sample is stored at 800C while a gas mixture of 67% H_2 and 33% N_2 is flowed at a rate of 75 sccm in

each channel. Once all the tests have been performed, the sample is cooled back to room temperature over a period of 800 minutes while flowing a gas mixture of 67% H_2 and 33% N_2.

The ITM sample is handled in a slightly different manner than the CoorsTek sample. In the case of the ITM sample, no reduction process is necessary. The ITM sample is also much more durable than the ceramic CoorsTek anode. However the ITM sample, being metal, is more susceptible to oxidation, especially at high temperatures. The ITM sample was heated within the experiment from room temperature to 800C over a period of 800 minutes to be consistent with the CoorsTek handling. Since fracture is not a concern with the ITM sample but oxidation is a concern, a gas mixture of 67% FG and 33% H_2 is flowed over the sample at a rate of 150 sccm in each channel. A gauge pressure of approximately 5 inH_2O is maintained in each channel. This allows for a highly reducing environment during the heating of the sample which helps prevent chemical oxidation. The slightly increased pressure helps to discourage any possible infiltration of O_2 from the atmosphere into the system. Once the sample reaches 800C the transport and reforming tests can be performed. In between tests the sample is stored at 800C while a gas mixture of 67% H_2 and 33% N_2 is flowed at a rate of 150 sccm in each channel at approximately 5 inH_2O gauge pressure. Once all tests have been performed the sample is cooled back to room temperature over a period of 800 minutes while a gas mixture of 67% H_2 and 33% N_2 is flowing at a rate of 150 sccm at approximately 5 inH_2O gauge pressure in each channel.

3.3.3 CO_2 transport experiments

CO_2 transport tests are used to measure the ability of gases to diffuse through a particular anode material. Three CO_2 transport runs were performed on each sample. The CO_2 transport tests are usually alternated with CO_2 dry reforming tests in the SAE. By alternating the tests, coking or other side effects of the previous reforming test that would affect mass transport within the sample will be seen in the results of the subsequent transport test.

In the transport experiments, a near-inert gas stream of 50% CO_2 and 50% forming gas (FG) (3.5% H_2 + 96.5% N_2) is fed to the electrolyte side gas manifold while a stream of pure FG is fed to the fuel side gas manifold. Total fuel flow rates are matched in each channel using MFCs. The gas pressures in each channel are equalized to each other using a water column. By equalizing the pressure in each gas channel, the pressure gradient across the sample is zero which better represents the operating conditions of an operational SOFC. Test runs are performed at four different flow rates (75, 100, 150 and 200 sccm per channel). The amount of CO_2 transported through the anode is determined by gas composition analysis of the fuel side exhaust using gas chromatography. The results of the

transport tests are then compared between samples. Samples with higher concentrations of CO_2 in the fuel side exhaust have higher gas transport capabilities.

3.3.4 Methane dry reforming tests

Fuel reforming experiments are performed utilizing a mixture of CH_4 and CO_2 at a typical SOFC operating temperature (800C). In the case of these experiments CO_2 represents the products of the electrochemistry reactions that would be present at the TPB during typical SOFC operation. Steam is not used as a reforming reactant due to poor humidity control and poor repeatability of results as detailed in Hecht et al.(E. Hecht, 2005). It has been established that the reforming reaction mechanisms between CO_2 reforming and steam reforming are essentially the same. As such, the CO_2 reforming performance can be extrapolated to qualitatively predict steam reforming performance of the sample. The use of CO_2 as primary reforming reactant is discussed in more detail in section 3.3.6.

For the dry reforming tests a mixture of 20% CH_4, 80% FG is supplied to the fuel-side inlet and a 50% CO_2, 50% FG mixture is supplied to the electrolyte-side inlet. The gases then diffuse through the porous sample and can participate in reforming reactions according to the reforming characteristics of the sample being tested. Total gas flow into each channel is matched. The gas pressures in each channel are equalized to each other using a water column. Exhaust stream gas compositions are measured using gas chromatography. Test runs are performed at four different input flow rates (75, 100, 150, 200 sccm per channel).

The exiting gas compositions are directly related to the internal reforming performance within the sample. The higher the concentration of reforming products in the exhaust streams, the higher internal reforming activity of the sample. Comparisons of the exhaust gas compositions allows for comparison of the reforming activity of each sample.

3.3.5 Experimental repeatability

CO_2 transport tests and CH_4 reforming tests are repeated three times for each sample to verify experimental repeatability. Each CO_2 transport test is followed by a CH_4 reforming test so that any decay in mass transport capabilities of the sample due to carbon deposition during the previous reforming test are seen in the subsequent CO_2 transport test. Only one test is performed in a 24 hour period. To avoid thermal stress on the samples and delays associated with cooling and reheating of the samples, they are maintained at 800C for the duration of the testing period. When not being tested, the CoorsTek anode is stored with mixture of 66% FG and 33% H_2 with a total flow of 75sccm in each gas channel at ambient pressure to maintain a reducing environment. The Plansee

ITM sample is stored with the same gas mixture but flowing at a higher rate of 150 sccm in each channel held at a pressure of approx 5 inH_2O using the water column. The storage parameters for the ITM sample are adjusted due to oxidation concerns. Each sample is held at operating temperature for approximately 6 days during the testing period, not including time to initially heat and cool the sample.

3.3.6 Discussion on the use of dry reforming

While steam is a critical reforming reactant and a product of the electrochemistry of SOFC operation, the use of steam in the experiment is extremely problematic. Hecht et al. report that the humidification level of the gas stream is extremely difficult to control, leading to poor repeatability of the reforming experiments that utilized steam as a reforming reactant (E. Hecht, 2005). A recent study by Sumi et al. compared the internal reforming capabilities of Ni-YSZ and Ni-ScSZ anodes both in steam reforming and dry reforming (CO_2) environments in this study Ni-ScSZ anode had higher reforming performance than the Ni-YSZ performance in both steam and dry reforming tests(H. Sumi, 2010). In a study for steam reforming and dry reforming of CH_4 Rostrup-Nielsen and Hansen note that the replacement of steam by CO_2 in the reforming reaction has no drastic impact on the reforming mechanism(Hansen, 1993). However both Sumi et al. and Rostrup-Nielsen and Hansen note that reforming activity using CO_2 is decreased when compared to steam reforming. This behaviour was also noted in Hecht et al.(E. Hecht, 2005).

While CO_2 reforming appears to be an acceptable proxy for steam reforming it is important to note that different reforming catalysts respond to dry reforming and steam reforming differently. Rostrup-Nielsen and Hansen note that the reforming activity ratio of steam reforming and dry reforming over Ni catalysts appears to be approximately 80%. However each other catalyst they tested had a different dry reforming to steam reforming activity ratio. It is extremely important to consider the dry reforming and steam reforming activity ratio when comparing anodes with different reforming catalysts in the SAE. While direct comparisons of dry reforming performance will always be possible when comparing the dry reforming results, trying to infer steam reforming activity based on dry reforming results is problematic. It is clear that the lack of steam reforming capabilities in the SAE is a significant issue and work is underway to add this capability to experiment.

4 COMPUTATIONAL MODEL

A computational model for the simulation of mass transport and chemical reactions occurring within the anode has been developed at the CFCC. Figure 6 shows a visual representation of the model framework.

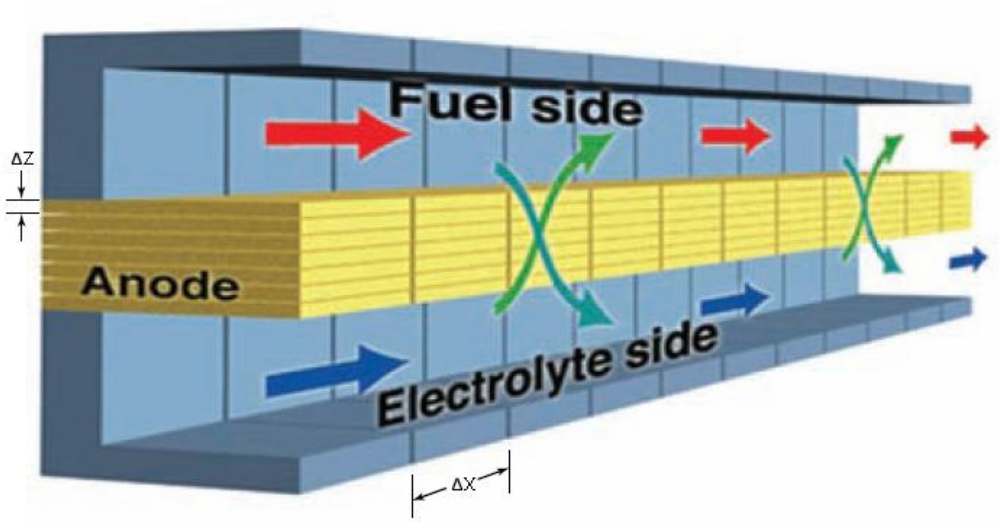

Figure 6- Frame work for the CFCC computational model. Anode and flow channels are divided into Δx elements along the length of the channel. The Anode is also divided into Δz elements through its thickness. Diagram taken from (E. Hecht, 2005)

Gas flow within the fuel and electrolyte channels is described by a series of perfectly stirred tank reactors. Gas flow within the anode is described by the Dusty-Gas Model (DGM). The flow within the flow channels is treated considering only axial variation in the x-direction. Perfect mixing is assumed within the flow channels. Plug-flow assumption is used within the anode. Therefore, only transport due to gradients in the z-direction is considered. Flow induced by axial gradients is neglected.

4.1 Flow in channels

Each channel is considered a series of perfectly stirred tank reactors, which implies uniform temperature and composition within the channel (H. Zhu, 2005). The continuity equation for gas species within the fuel channel can be seen below in equation 4.1.

$$\dot{m}_k^{\ddagger} = \dot{m}_k + j_k^c A_c \tag{4.1}$$

Where $\dot{m}_k^{\ddagger}$ and $\dot{m}_k$ are the mass flow rates in and out of the x-direction channel element respectively, j_k^c is the mass flux of the species *k* in the *z*-direction from the channel into the anode resulting from the chemistry and transport occurring within it, and A_c is the cross-sectional area between the fuel channel and anode control volume. The general continuity equation within the fuel channel is shown below.

$$\dot{m}^{\ddagger} = \dot{m}_k + \sum_{k=1}^{K} j_k^c A_c \tag{4.2}$$

K is the total number of species present in the gas mixture and

$$\dot{m}_k = Y_k \dot{m} \tag{4.3}$$

Where Y_k is the species mass fraction.

The continuity equation is used to solve for the density of the gas mixture.

The flow channels are assumed to be chemically inert and the gas phase chemistry within the channels is assumed to be negligible. With the short residence times of the SAE taken it to account, it has been shown that neglecting the gas phase chemistry is reasonable under the operating conditions of the (800 C, 1 Atm pressure) (G.K. Gupta, 2006).

4.2 Transport and chemistry within porous anode

The gas composition within the anode is determined by solving a reactive porous media problem in the structure of the anode itself. The single species continuity equation in the anode is shown in equation (4.4),

$$\frac{\delta j_k}{\delta z} = \dot{s_k} W_k A_s \tag{4.4}$$

where j_k is the mass flux of species *k* within the anode, A_s is the specific area (i.e., area per unit volume) of the exposed Ni catalyst, $\dot{s_k}$ is the net molar production rate of gas-phase species k by heterogeneous reforming chemistry, and W_k are the species molecular weights (R.J. Kee, 2003). The general continuity equation (equation 4.5) shown below is then used to find the density (ρ) of the gas mixture.

$$\sum_{k=1}^{K} \frac{\delta j_k}{\delta z} = \sum_{k=1}^{K} \dot{s}_k W_k A_s \tag{4.5}$$

Gas species fluxes within the anode are related by the Dusty-Gas Model (DGM) (Malinauskas, 1983),(H. Zhu, 2005) .

The DGM is an implicit relationship between the gas-phase molar fluxes of each species, J_k, the molar concentrations $[X_k]$, concentration gradients, and the pressure gradient *p*. The DGM is shown the equation below.

$$\sum_{l \neq k} \frac{[X_l]J_l - [X_k]J_l}{[X_T]D_{kl}^e} + \frac{J_k}{D_{k,Kn}^e} = -\nabla[X_k] - \frac{[X_k]}{D_{k,Kn}^e} \frac{B_g}{\mu} \nabla p \tag{4.6}$$

B_g is the permeability, μ is the mixture viscosity and $[X_T]$ is the total molar concentration, as shown below.

$$[X_T] = \frac{p}{RT} \tag{4.7}$$

The DGM is the combination of ordinary multi-component diffusion (gas-gas collisions), Knudsen diffusion (gas-wall collisions), and pressure-driven Darcy flow. The ordinary diffusion coefficient and the Knudsen diffusion coefficient depend on the binary gas-to-gas diffusion coefficients

(evaluated from kinetic theory) and the physical porous media properties. These properties include porosity ϕ, average pore radius r_p, and tortuosity τ_g.

Heterogeneous chemistry within the anode is represented by a reaction mechanism describing CH_4-reforming on Ni-based catalysts. The mechanism used is taken from Hecht et al. and contains 42 irreversible elementary reactions (see Table 2) involving six gas-phase and twelve surface- adsorbed species (E. Hecht, 2005). Because the mechanism is based on elementary reactions and describes all combinations of steam reforming, dry reforming, partial oxidation, and autothermal reforming, its applicability spans a far-broader range than the global reforming reactions often used in SOFC internal reforming modelling.

Since the pore size within the anode is comparable to the molecular mean-free-path length, the probability for gas-gas collisions is low. Gas-phase chemistry within the voids of the anode can therefore be neglected(E. Hecht, 2005).

Table 2- Surface reaction mechanism for CH_4 on Ni(E. Hecht, 2005)

	Reaction	A^a	n	E^a
1.	$H_2 + Ni(s) + Ni(s) \rightarrow H(s) + H(s)$	1.000E-02[b]	0.0	0.00
2.	$H(s) + H(s) \rightarrow Ni(s) + Ni(s) + H_2$	5.593E+19[b]	0.0	88.12
3.	$O_2 + Ni(s) + Ni(s) \rightarrow O(s) + O(s)$	1.000E-02[b]	0.0	0.00
4.	$O(s) + O(s) \rightarrow Ni(s) + Ni(s) + O_2$	2.508E+23[b]	0.0	470.39
5.	$CH_4 + Ni(s) \rightarrow CH_4(s)$	8.000E-03[b]	0.0	0.00
6.	$CH_4(s) \rightarrow Ni(s) + CH_4$	5.302E+15[b]	0.0	33.15
7.	$H_2O + Ni(s) \rightarrow H_2O(s)$	1.000E-01[b]	0.0	0.00
8.	$H_2O(s) \rightarrow Ni(s) + H_2O$	4.579E+12[b]	0.0	62.68
9.	$CO_2 + Ni(s) \rightarrow CO_2(s)$	1.000E-05[b]	0.0	0.00
10.	$CO_2(s) \rightarrow Ni(s) + CO_2$	9.334E+07[b]	0.0	28.80
11.	$CO + Ni(s) \rightarrow CO(s)$	5.000E-01[b]	0.0	0.00
12.	$CO(s) \rightarrow Ni(s) + CO$	4.041E+11[b]	0.0	112.85
		$\varepsilon_{CO(s)}$	0.0	-50.0[c]
13.	$O(s) + H(s) \rightarrow OH(s) + Ni(s)$	5.000E+22	0.0	97.90
14.	$OH(s) + Ni(s) \rightarrow O(s) + H(s)$	2.005E+21	0.0	37.19
15.	$OH(s) + H(s) \rightarrow H_2O(s) + Ni(s)$	2.005E+21	0.0	42.70
16.	$H_2O(s) + Ni(s) \rightarrow OH(s) + H(s)$	2.175E+2	0.0	91.36
17.	$OH(s) + OH(s) \rightarrow O(s) + H_2O(s)$	3.000E+21	0.0	100.00
18.	$O(s) + H_2O(s) \rightarrow OH(s) + OH(s)$	5.423E+23	0.0	209.37
19.	$O(s) + C(s) \rightarrow CO(s) + Ni(s)$	5.200E+23	0.0	148.10
20.	$CO(s) + Ni(s) \rightarrow O(s) + C(s)$	1.418E+22	0.0	115.97
		$\varepsilon_{CO(s)}$		-50.0[c]
21.	$O(s) + CO(s) \rightarrow CO_2(s) + Ni(s)$	2.000E+19	0.0	123.60
22.	$CO_2(s) + Ni(s) \rightarrow O(s) + CO(s)$	3.214E+23	-1.0	86.50
23.	$HCO(s) + Ni(s) \rightarrow CO(s) + H(s)$	3.700E+21	0.0	0.0
24.	$CO + H(s) \rightarrow HCO(s) + Ni(s)$	2.338E+20	-1.0	127.98
25.	$HCO(s) + Ni(s) \rightarrow O(s) + CH(s)$	2.338E+20	-3.0	95.80
26.	$O(s) + CH(s) \rightarrow HCO(s) + Ni(s)$	7.914E+20	-3.0	114.22
27.	$CH_4(s) + Ni(s) \rightarrow CH_3(s) + H(s)$	3.700E+21	0.0	57.70
28.	$CH_3(s) + H(s) \rightarrow CH_4(s) + Ni(s)$	4.438E+21	0.0	58.83
29.	$CH_3(s) + Ni(s) \rightarrow CH_2(s) + H(s)$	3.700E+24	0.0	100.00
30.	$CH_2(s) + H(s) \rightarrow CH_3(s) + Ni(s)$	9.513E+22	0.0	52.58
31.	$CH_2(s) + Ni(s) \rightarrow CH(s) + H(s)$	3.700E+24	0.0	97.10
32.	$CH(s) + H(s) \rightarrow CH_2(s) + Ni(s)$	3.008E+24	0.0	76.43
33.	$CH(s) + Ni(s) \rightarrow C(s) + H(s)$	3.700E+21	0.0	18.80
34.	$C(s) + H(s) \rightarrow CH(s) + Ni(s)$	4.400E+22	0.0	160.49
35.	$O(s) + CH_4(s) \rightarrow CH_3(s) + OH(s)$	1.700E+24	0.0	88.30
36.	$CH_3(s) + OH(s) \rightarrow O(s) + CH_4(s)$	8.178E+22	0.0	28.72
37.	$O(s) + CH_3(s) \rightarrow CH_2(s) + OH(s)$	3.700E+24	0.0	130.10
38.	$CH_2(s) + OH(s) \rightarrow O(s) + CH_3(s)$	3.815E+21	0.0	21.97
39.	$O(s) + CH_2(s) \rightarrow CH(s) + OH(s)$	3.700E+24	0.0	126.80
40.	$CH(s) + OH(s) \rightarrow O(s) + CH_2(s)$	1.206E+23	0.0	45.42
41.	$O(s) + CH(s) \rightarrow C(s) + OH(s)$	3.700E+21	0.0	48.10
42.	$C(s) + OH(s) \rightarrow O(s) + CH(s)$	1.764E+21	0.0	129.08

[a] Arrhenius parameters for the rate constants written in the form:

$k = A\exp(-E/RT)$. The units of A are given in terms of moles, centimeters, and seconds. E is in kJ/mol.

[b] Sticking coefficient

[c] Coverage dependent activation energy. Detailed definition may be found in Hecht et al. Total available surface site density is $\Gamma = 2.60 \times 10^{-9}$ mol/cm^2 .

4.3 Computational algorithm

The resulting series of nonlinear simultaneous equations is solved computationally. The species continuity equations for the gas channels are coupled to the anode species continuity equations by the exchanged mass fluxes j_k^c exchanged between the anode and flow channels. Equation 4.6 is a second-order boundary value problem, with the gas-phase species compositions in the channels taken as the boundary conditions.

Due to the uniform gas channel assumptions, the compositions at the top and bottom of the anode are taken to be the compositions within the gas flow channels. There is assumed to be no flow resistance between the anode surface and the gas channels. The channels are divided into cells of length Δx and the anode is divided into cells of length Δz. The pressure within the anode is calculated using the ideal gas law below.

$$\rho = \frac{P\bar{W}}{RT} \tag{4.8}$$

Where P is pressure, $\bar{W}$ is the average molecular weight, R is the universal gas constant, and T is temperature. The temperature is assumed to be uniform through the channel and determined by the temperature of the external furnace. Fuel flow is assumed to be isobaric. These assumptions have been verified by measurements made during experimentation.

The CFCC computational model was originally developed and reported by Hecht et al. (E. Hecht, 2005). The model as described above has been completely rewritten with modifications to gas phase uniformity assumptions and the computational algorithm. The model used in this report is written by Amy Richards at the CFCC. The above description of the model is based extensively on a report from Amy Richards (Richards, 2010). All model fitting to the experimental SAE results in this report was performed by Amy Richards.

5 EXPERIMENTAL RESULTS

5.1 Visual observations pre and post run

Pre and post run pictures of the CoorsTek and the ITM samples can be seen in Figure 7. Significant differences in the samples can be seen. Prior to running in the SAE, the CoorsTek is in a non-reduced state. The NiO is still present in the CoorsTek anode giving it a green color. After the SAE experiment it can be seen that the NiO has been reduced to Ni as the anode is a uniform grey color.

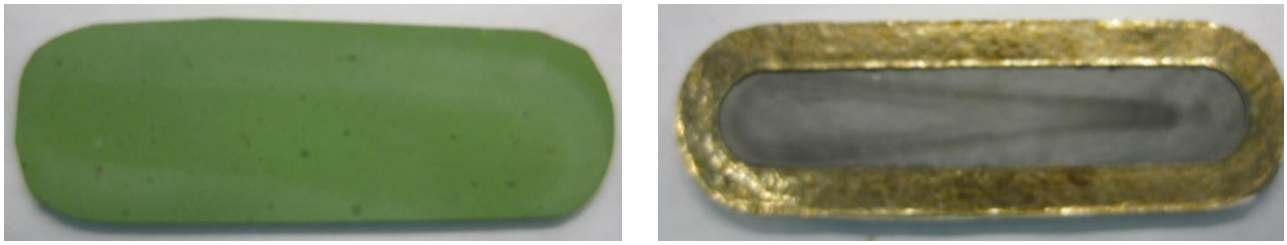

Figure 7-Images of CoorsTek Ni-YSZ anode. Left: CoorsTek anode prior to being run in the SAE. Green color is unreduced NiO. Right: CoorsTek anode after running the SAE, gray color indicates NiO is completely reduced to Ni. The gold ring around the sample is the mica seal from the SAE experiment, which is now adhered to the surface.

Pictures of the Plansee ITM sample pre and post run can be seen in Figure 8. The ITM sample also experiences a significant color change. Prior to running in the SAE, the ITM sample is a uniform grey color. After the SAE experimentation, the ITM sample has turned black. The color change is assumed due to the growth of an oxidation layer.

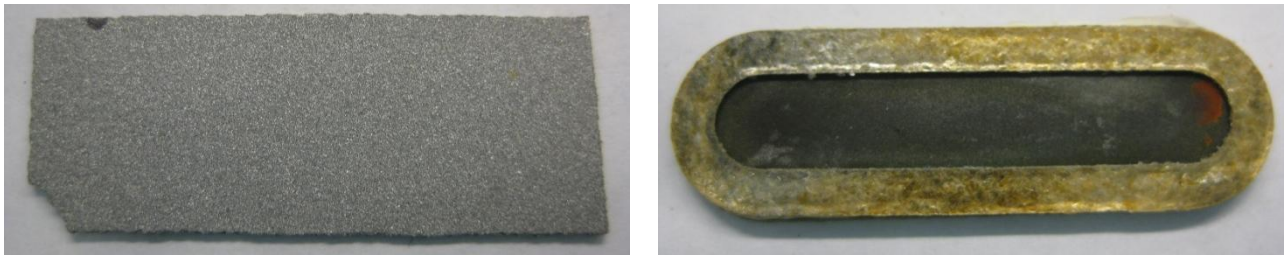

Figure 8- Images of Plansee ITM support. Left: Raw ITM prior to final forming. Right: ITM after running in the SAE, the black color is an oxidation layer on the sample. The gold ring around the sample is the mica seal from the SAE experiment, which is now adhered to the surface.

Cross-sectional images of the post run ITM and CoorsTek sample can be seen in Figure 9. The Plansee sample shows uniform oxidation through the sample. The CoorsTek sample shows uniform reduction of the NiO through the cross-sectional direction of the sample. NiO is still present on the left and right sides of the sample suggesting that the sealing techniques employed in the SAE work satisfactorily. Note that the CoorsTek sample pictured is from an abbreviated run in the SAE and it is likely that the NiO remaining in a sample that had run for an entire testing cycle would show significantly less NiO remaining.

Figure 9-Cross-sectional images of the samples after running in the SAE. Left: The Plansee ITM sample shows uniform oxidation through the entire crossection. Right: The CoorsTek Ni-YSZ show uniform reduction of NiO through the thickness of the sample, NiO remains laterally, suggesting effective edge sealing. Note: the CoorsTek sample pictured was only run in the SAE for a short time, complete reduction of NiO is expected in samples that have received full term testing.

5.2 Porosimetry results

Two different porosimetry measurement techniques are used in this report, liquid picnometry (Archimedes' method) using standard DI water as the fluid and mercury porosimetry. Liquid picnometry measurements are conducted at the CFCC. Mercury porosimetry measurements are conducted by a third party, Micromeritics Particle Analysis (Norcross, GA).

5.2.1 Liquid picnometry results

Three samples of the Ni-YSZ anode and three samples of the ITM support were measured using Archimedes' method. Referring to Table 3 it can be seen that the ITM and Ni-YSZ anode have similar porosities when measured using Archimedes method.

Table 3- Porosimetry results

	Archimedes	Mercury porosimetry		
Sample	Porosity	Porosity	Ave. Pore Diameter (μm)	Pore size distribution (μm)
Ctek#1*	40.3%	38.42%	0.58	0.9-3
Ctek#2*		48.63%	1.81	0.3-0.9
ITM	42.5%	41.69%	17.13	10-100

* Two CoorsTek samples were sent to Micromeritics due to poor repeatability, neither result appears to be correct when compared to the SEM analysis and computational model fitting parameters.

5.2.2 Mercury porosimetry results

Mercury porosimetry measurements in this report are performed by Micromeritics Particle Analysis. Due to poor repeatability, the Ni-YSZ sample was repeated. Figure 10 shows the comparison of the cumulative mercury intrusion for the Ni-YSZ samples. The first sample suggests a pore diameter distribution from 0.3-0.9μm while the second sample suggests a distribution from 0.9-3μm. Comparing to SEM results in the next section, the larger pore size distribution appears to be more accurate. Unfortunately, referring to Table 3, it can be seen that while the pore sizing is more accurate, the reported porosity is inconsistent with the results from the liquid picnometry tests. The cause of the discrepancy is not clear.

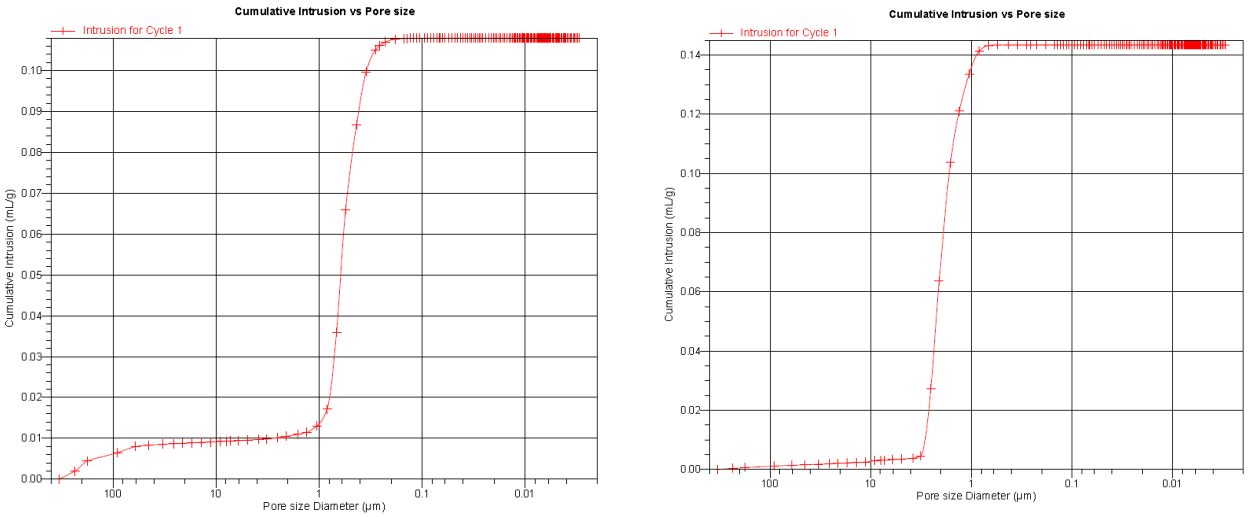

Figure 10- Mercury intrusion data for CoorsTek NiYSZ Left: Intrusion data from sample #1 Right: Intrusion from sample #2. Data provided by Micromeritics (Norcross, GA)

Figure 11 shows the cumulative mercury intrusion of the ITM sample. Intrusion data from the ITM sample suggests a pore size distribution from 10-100µm and porosity of 41.7% which is consistent with the liquid picnometry results.

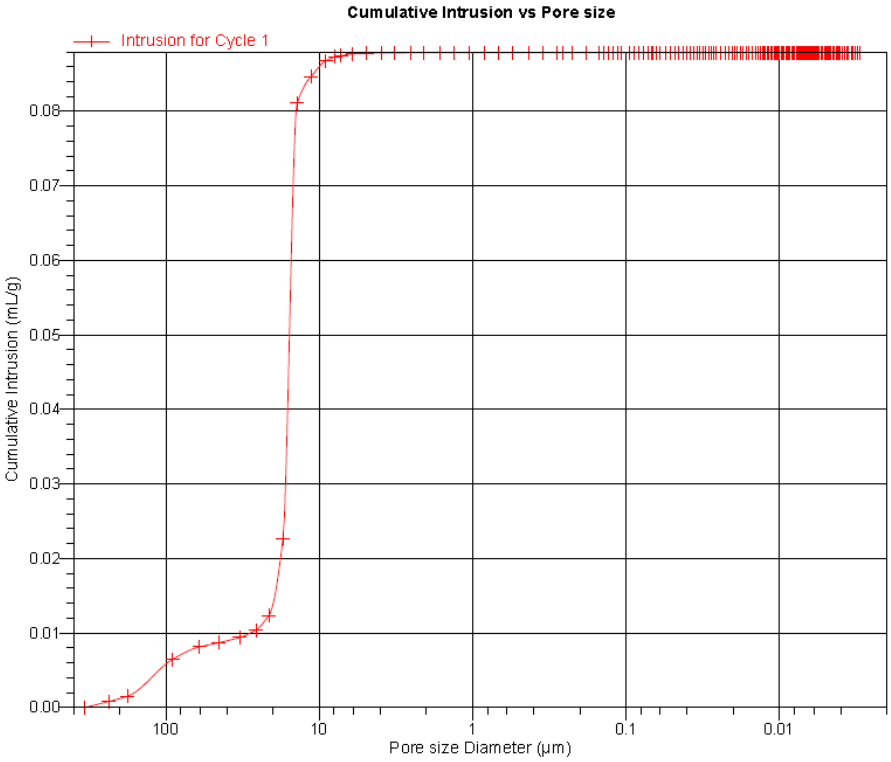

Figure 11-Mercury intrusion data from ITM sample. Data provided by Micromeritics (Norcross, GA)

5.3 SEM analysis

SEM images taken of the cross sections and surfaces of each sample are shown at various magnifications in Figure 12 and Figure 13 respectfully. As can be seen, the samples are extremely different in structure and morphology. Open porosity of the anode or support is critical as it provides the needed pathways for the fuels to enter and the exhausts to exit the fuel cell. As shown above in the porosity results, each sample has roughly the same volume porosity but drastically different pore size and particle size. Referring to Figure 12 and Figure 13, the CoorsTek anode is characterized by much finer particle size and pore structure than the ITM support. The larger pore size of the ITM support promotes increased permeability which one would expect to increase the transport capabilities of the support when compared to the CoorsTek anode.

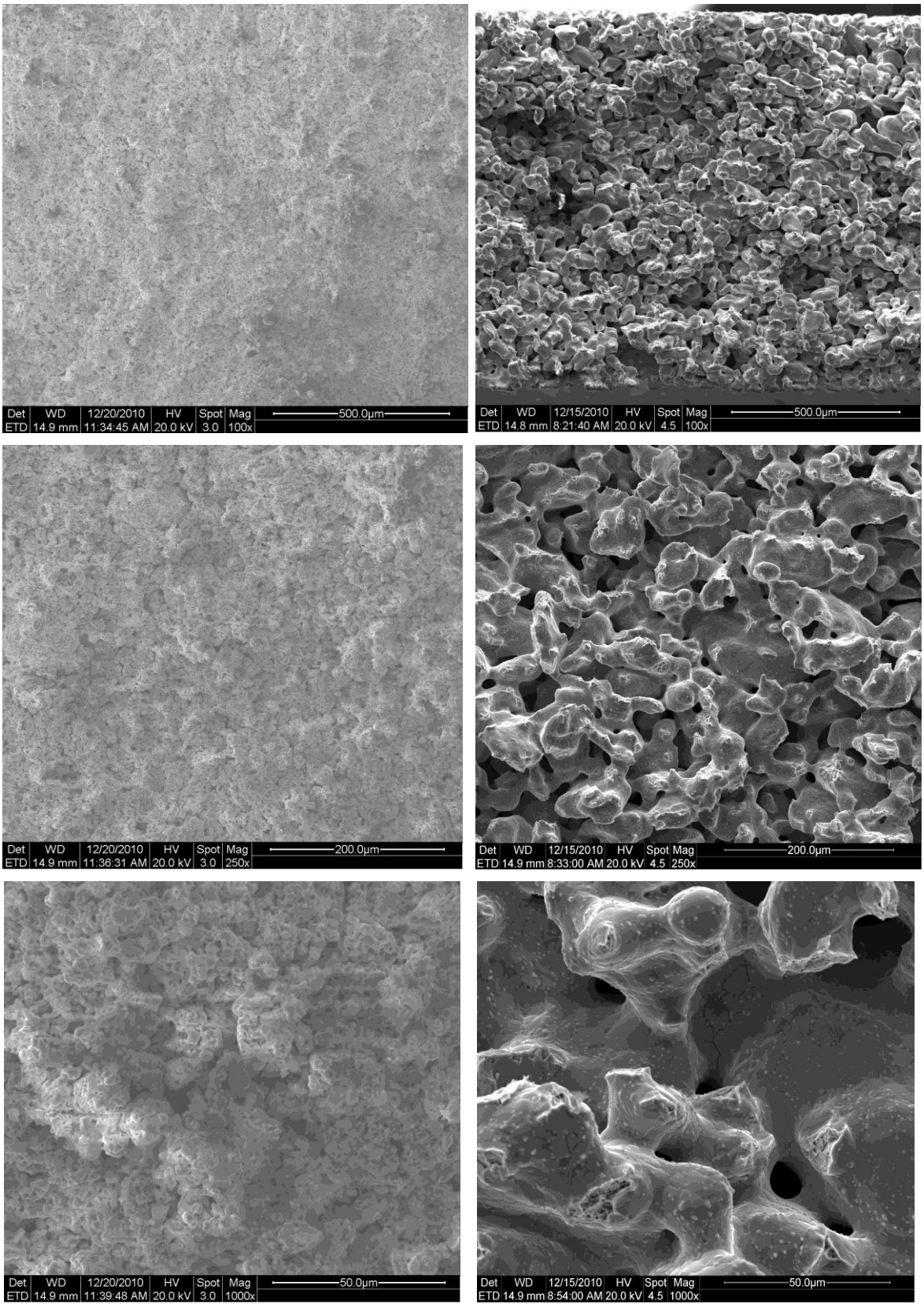

Figure 12- Cross-sectional images of the of the Ni-YSZ and ITM sample. Left column: Reduced CoorsTek Ni-YSZ. Right column: Plansee ITM

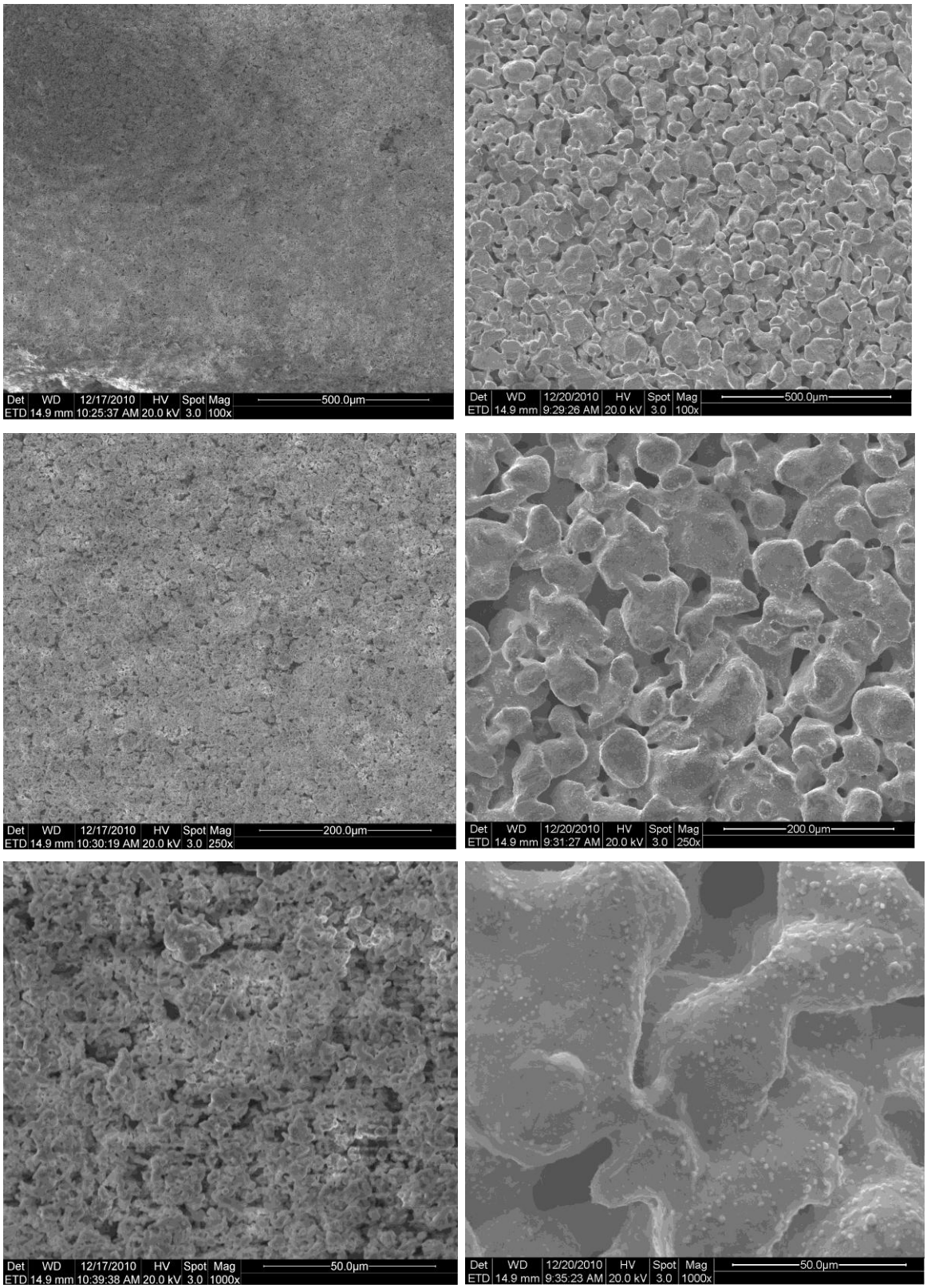

Figure 13- Surface images of the of the Ni-YSZ and ITM samples. Left column: Reduced CoorsTek Ni-YSZ. Right column: Plansee ITM

5.3.1 Pre Run Plansee ITM support compared to post run ITM support

As shown above in section 5.1, even after the short testing period associated with the SAE, the ITM sample shows signs of oxidation. SEM images of the surface and cross section of the ITM material pre and post run in the SAE can be seen in Figure 14 and Figure 15 respectfully. While there is no significant change in the cross sectional or surface morphology evidence of a thin oxidation layer can be seen on the post run images.

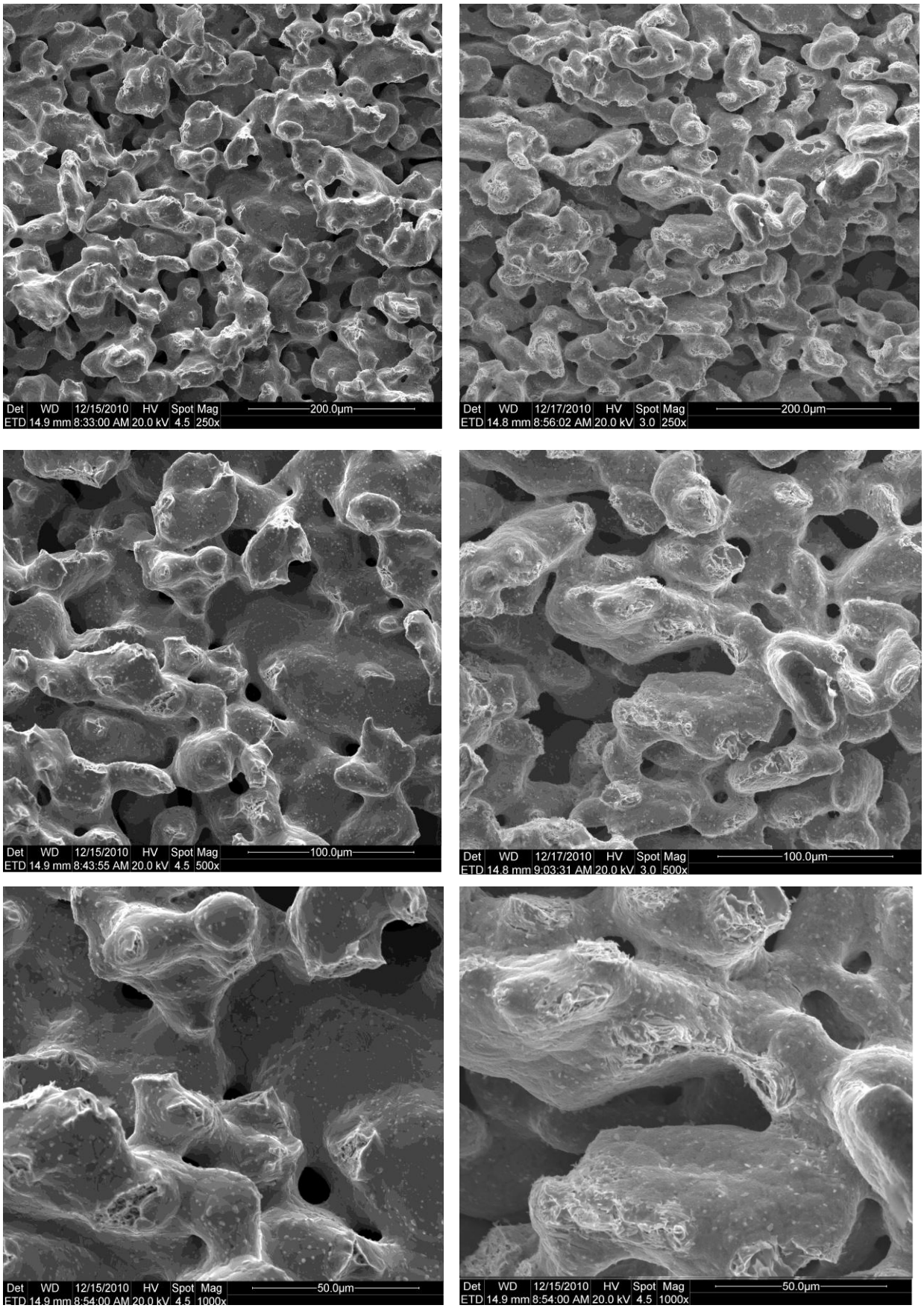

Figure 14- Cross-sectional images of Plansee ITM pre and post run in the SAE. Right column: Prerun ITM. Left column: Post run ITM, evidence of a thin oxidation layer can be seen.

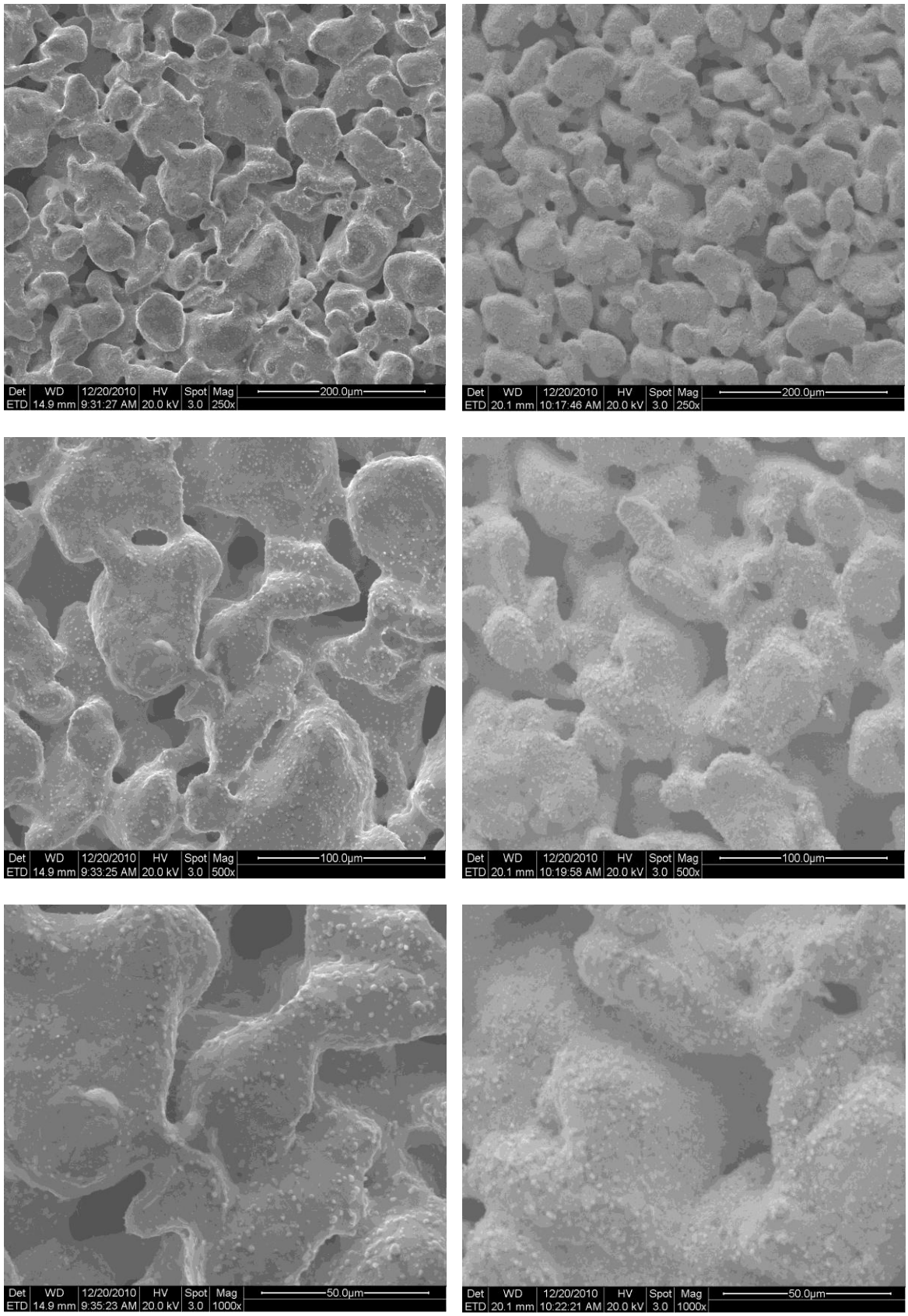

Figure 15- Surface images of Plansee ITM pre and post run in the SAE. Right column: Prerun ITM. Left column: Post run ITM, evidence of a thin oxidation layer can be seen.

5.4 Separated anode experiment results

As described in section 3.3.1 the internal reforming and transport properties of the samples are tested using the SAE. Results for the SAE are separated into two sections, CO_2 transport and CH_4 reforming.

5.4.1 SAE CO_2 transport results

In the CO_2 transport test, the fuel side manifold is supplied with a 100% FG mixture (3.5% H_2 +96.5% N_2). The electrolyte side gas manifold is supplied with a 50% FG and 50% CO_2 mixture. The gases are allowed to diffuse across the sample according to its specific transport properties. Therefore, the amount of CO_2 that diffused to the fuel side of the sample is related to the transport capabilities of the sample. By comparing the CO_2 concentration present in the fuel side exhaust stream in each sample, a comparison of the mass transport characteristics of the different samples can be made.

Figure 16 shows the CO_2 mole fraction present in the fuel side exhaust of both the ITM and CoorsTek samples. CO_2 concentration in the exhaust stream of the 1mm thick ITM sample is approximately 17% higher than the 1.4mm thick CoorsTek sample, suggesting slightly increased mass transport characteristics for the ITM support. However the CoorsTek sample is 40% thicker than the ITM sample.

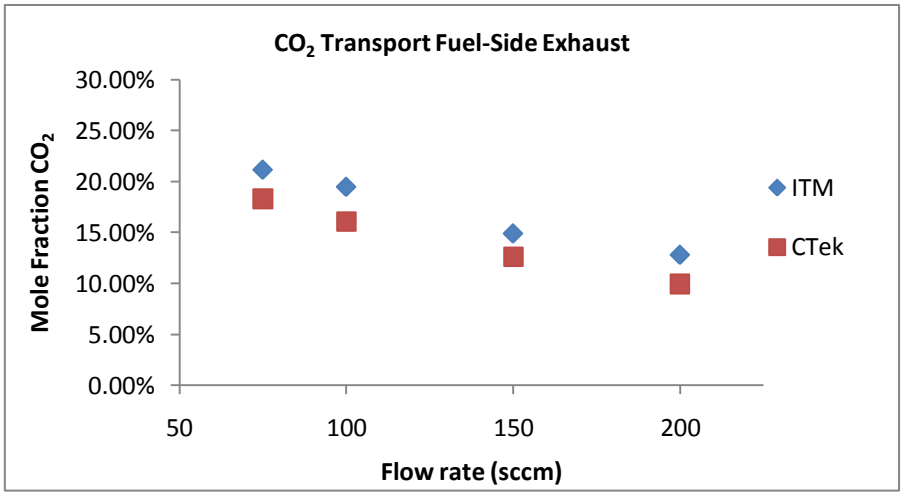

Figure 16- CO_2 transport, fuel side CO_2 mole fraction for Ni-YSZ and ITM samples

Examining exhaust gas compositions more closely, it can be seen that a small amount of carbon monoxide (CO) gas is present in the CoorsTek fuel side and electrolyte side exhaust but not present in the ITM exhaust (Figure 17). Since CO is not present in the supply gas mixture it must be a product of a gas phase chemical reaction within the CoorsTek anode itself.

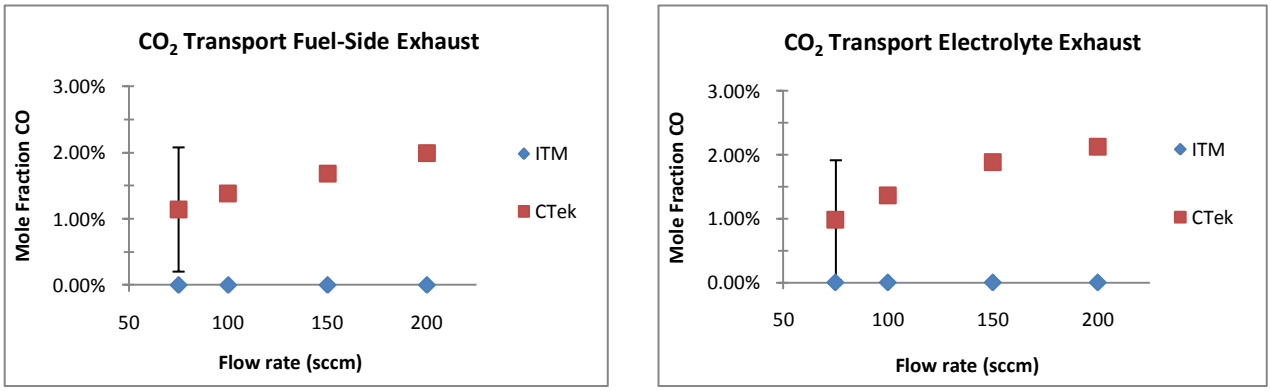

Figure 17- CO_2 transport, CO Mole fraction in SAE exhaust streams of Ni-YSZ and ITM sample Left: Fuel-side exhaust. Right: Electrolyte-side exhaust

The H_2 concentration in the fuel side and electrolyte side for both samples is shown in Figure 18. Examining the exiting hydrogen concentrations of the samples, it is clear that the CoorsTek sample has significantly lower hydrogen content. Since both samples are supplied with the same gas mixtures it is clear that the hydrogen in the CoorsTek anode as been consumed by a gas phase chemical reaction

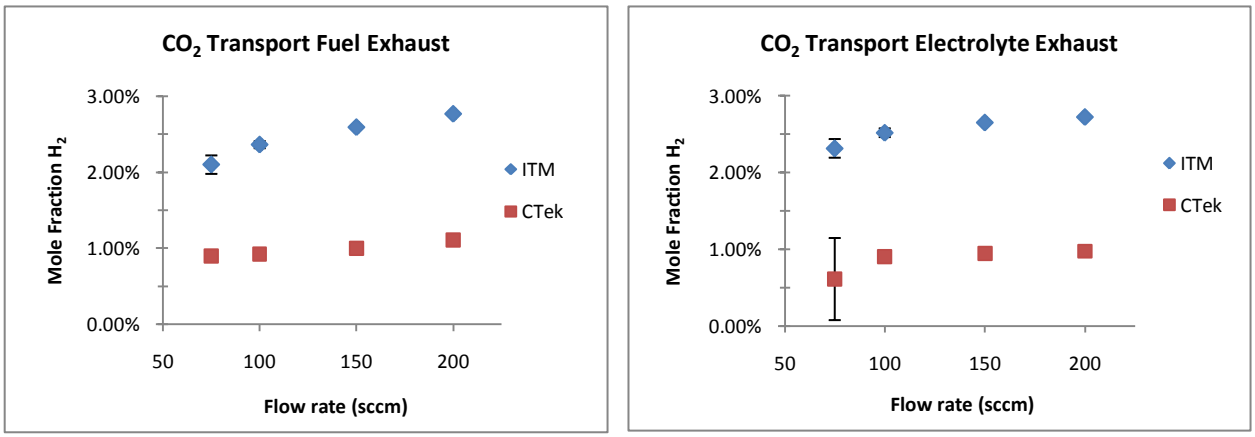

Figure 18- CO_2 transport, H_2 mole fraction in SAE exhaust streams of Ni-YSZ and ITM sample Left: Fuel-side exhaust. Right: Electrolyte-side exhaust

The presence of CO and the consumption of H_2 within the CoorsTek exhaust stream strongly suggests the presence of a gas phase, reverse water gas shift (RWGS) reaction taking place within the CoorsTek anode. The chemical equation for the reverse water gas shift reaction can be seen below (equation 5.1).

$$H_2 + CO_2 \rightarrow CO + H_2O \tag{5.1}$$

The presence of the RWGS reaction within the CoorsTek anode complicates the analysis of the CO_2 transport results. From equation 5.1 it can be seen that H_2 and CO_2 react to form H_2O and CO. No H_2O is measured in the exhaust stream because H_2O is removed from the exhaust stream by the counter flow dryer prior to arriving at the GC. Due to the presence of the RWGS reaction in the CoorsTek anode the resulting concentration of CO_2 in the exhaust stream is lower than expected, when assuming inert gas phase chemistry. Also, since the H_2O is removed from the gas stream prior to the GC, the reported mole fractions of the exhaust gas components are incorrect because of the missing H_2O species. Fortunately, it is possible to compensate for the RWGS shift by using the stoichiometry of the reaction. As the consumption of CO_2 and the production of CO occur at a 1:1 molar ratio, the CO_2 concentration in the CoorsTek exhaust stream can be adjusted by adding the reported CO concentration to the reported CO_2 concentration providing a "total carbon" (TC) concentration measurement. Also, as the production of CO occurs at a 1:1 molar ratio with H_2O, the reported CO concentration can be taken as the resulting H_2O concentration. The reported mole fractions are renormalized assuming H_2O to be present in a concentration equal to the concentration of CO. Figure 19 shows the CO_2 transport corrected results for the CoorsTek and ITM samples.

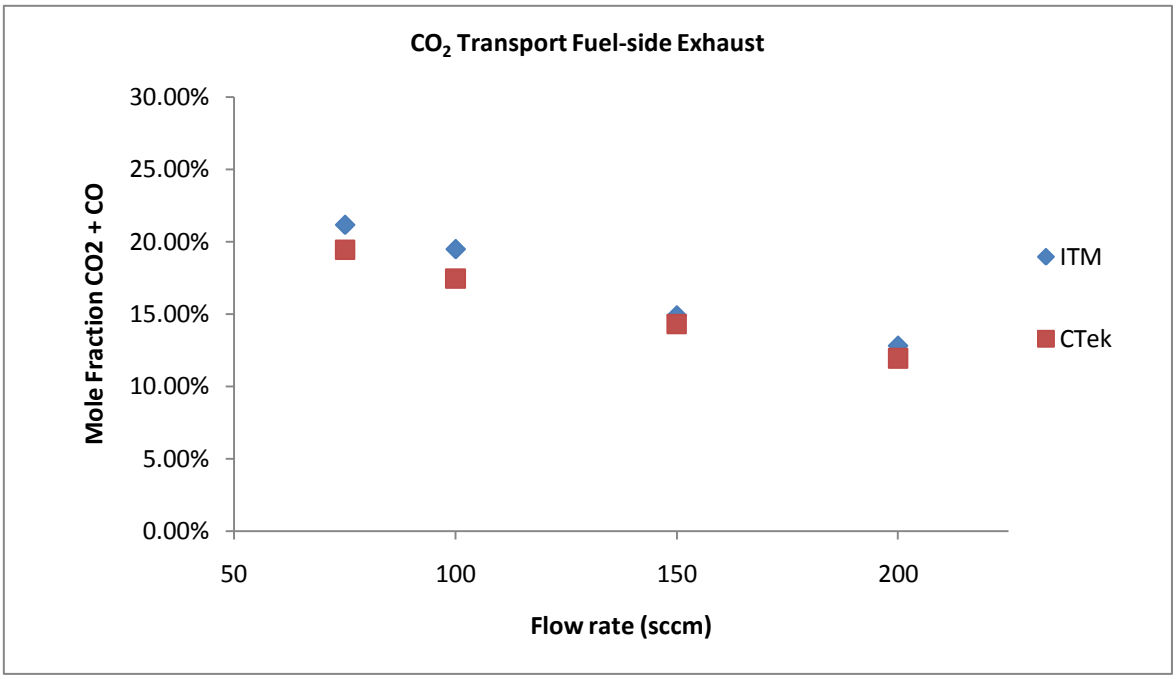

Figure 19- CO_2 Transport, Corrected "Total Carbon" transport for each sample.

As can be seen in Figure 19 the adjusted transport performance of the samples is very comparable. On average the ITM sample is within 6% of the CoorsTek sample, which is remarkable considering the differences in the thickness and morphologies of the two samples.

5.4.2 CO_2 transport model results

Using the sample porosity and thickness as constants, the CFCC computational model is fit to the SAE data at a single flow rate by using an iterative approach adjusting sample tortuosity as a fitting parameter. Once the most appropriate tortuosity is found, the model is used to calculate the gas compositions at the other flow rates. Computational fitting for the SAE data in this report was performed by Amy Richards at the CFCC. The fitting parameters used for the CorrsTek and ITM samples can be seen in Table 4.

Table 4- Morphological properties of samples used in AFL model fitting

Sample	Porosity	Mean Pore Radius (μm)	Mean Particle Diameter (μm)	Specific Catalyst Sfc Area (1/m)	Thickness (mm)	Tortuosity
CoorsTek Ni-YSZ	41%	0.9	1	150000	1.45	5.8
Plansee ITM	41.7%	8.6	65	0	1.0	7.6

The model fit to the CoorsTek CO_2 transport results can be seen in Figure 20 and Figure 21. The model fit to the ITM CO_2 transport results can be seen in Figure 22 and Figure 23. The model fit to the CoorsTek sample is quite good, all predicted species are within approximately 3% of their measured values with the SAE. The model fit for the ITM is not as good as the CoorsTek data; however, the overall trends between the model and SAE data are in agreement. The model predicts approximately 10-15% higher CO_2 concentration in the fuel side exhaust of the ITM sample, thus predicting higher transport performance than what was observed in the SAE.

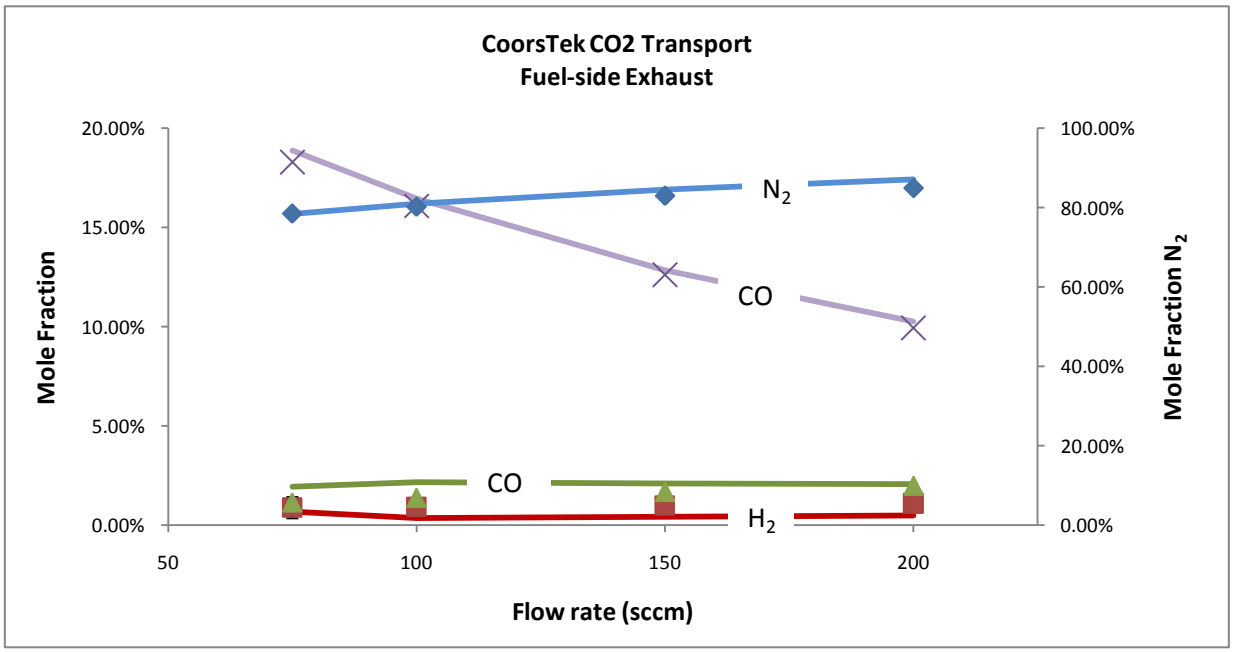

Figure 20- CO_2 transport CoorsTek fuel-side exhaust composition. SAE measurements represented by data points, modeling results are represented by solid lines.

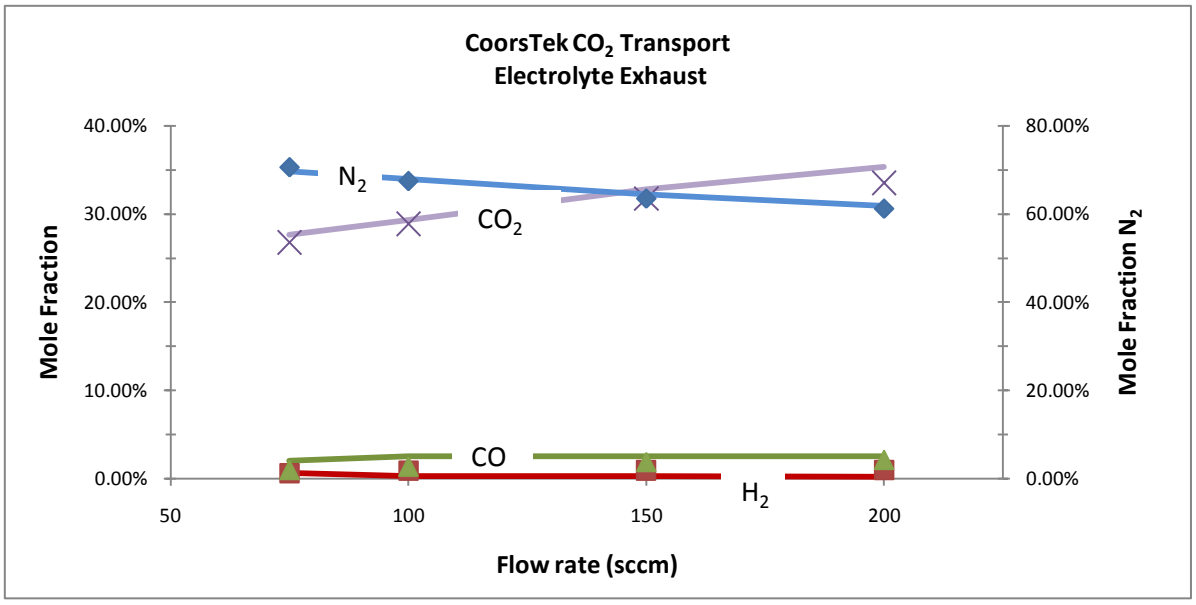

Figure 21- CO_2 transport CoorsTek electrolyte-side exhaust composition. SAE measurements represented by data points, modeling results are represented by solid lines.

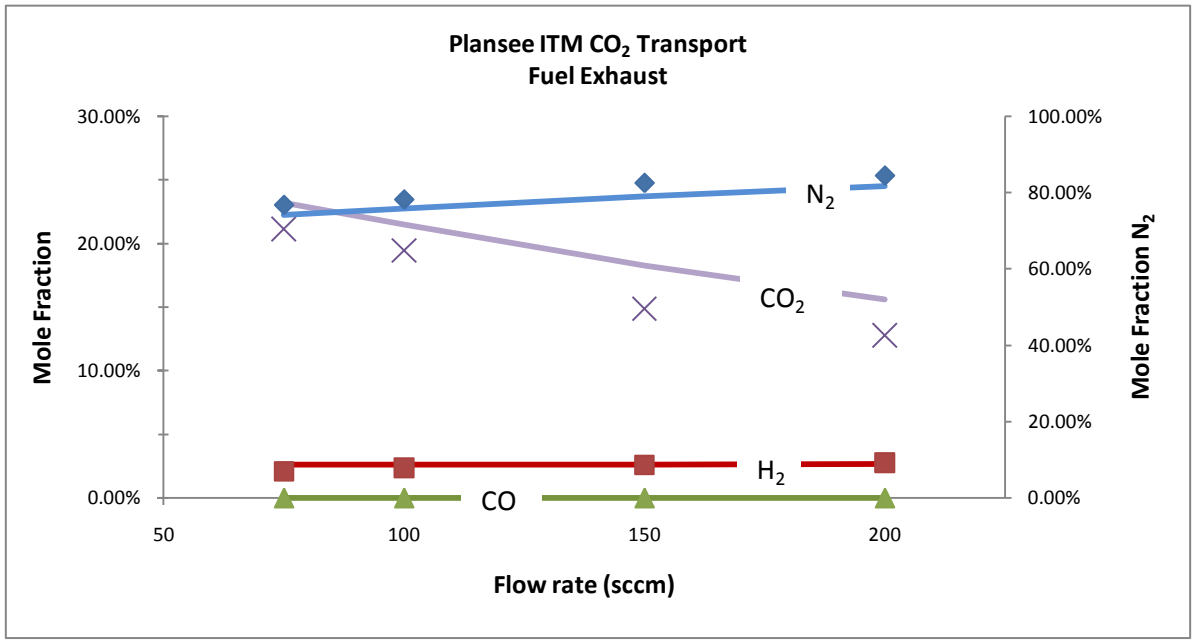

Figure 22- CO_2 transport Plansee ITM fuel-side exhaust composition. SAE measurements represented by data points, modeling results are represented by solid lines.

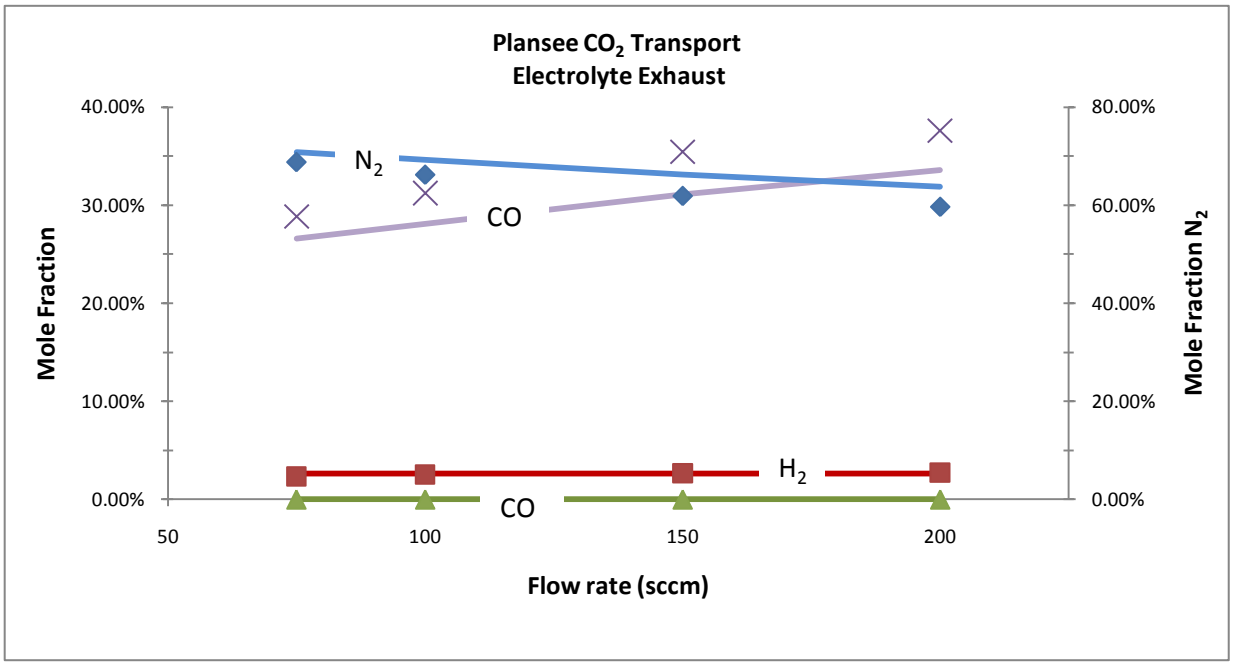

Figure 23 - CO_2 transport Plansee ITM electrolyte-side exhaust composition. SAE measurements represented by data points, modeling results are represented by solid lines.

There are some possible explanations for the discrepancy between the model and SAE results for the ITM sample. While the fuel channel is being sampled by the GC, the electrolyte channel is venting to atmosphere, resulting in a significant pressure gradient across the sample due to gas flow resistance associated with the GC measurement. The computational model assumes a zero pressure gradient across the sample. The SAE uses a water column to minimize this pressure gradient. By venting to atmosphere through the water column a back pressure equivalent to the height of the water above the inlet to the water column is applied to the venting gas channel. Pressure meters located on each gas channel are monitored and the water height in the column is adjusted until the meters read an equivalent pressure, thus eliminating the pressure gradient across the porous sample. If the gas meters attached to each channel were poorly calibrated, or if the pressure were poorly balanced, a pressure gradient would still be present across the sample. Due to a significantly larger pore size, the ITM would be much more susceptible to these pressure gradients. Comparing the CO_2 concentrations in the fuel side exhaust to the model results, the difference between the two is consistent with a higher pressure in the fuel channel, thus retarding the CO_2 transport to that side. Human error in balancing the pressure seems unlikely as the difference between the model and measured data is consistent at all flow rates. The fact that the model is consistently higher than the measured results suggests a more systematic error, for example, poor meter calibration.

Another possible explanation for the mismatch between the experimental data and the model results resides on a fundamental assumption upon which the model was constructed. The DGM assumes that perfect spheres stacked on one another constitute the interior morphology of the sample. Review of the SEM analysis clearly indicates that this is a poor assumption for both the CoorsTek and ITM samples. The CoorsTek sample however has a much more uniform and finer morphology than the Plansee ITM. The ITM sample has significantly larger particle sizes and larger pore sizes than the CoorsTek sample. In addition the distribution of the sizes appears to be greater as well. The larger distribution of the particle and pore sizing leads to a more random internal morphology. It is reasonable to assume that increased randomness of the sample's interior morphology invalidates the perfect sphere assumption of the DGM. Increased randomness within the sample would decrease transport performance of the sample, which is consistent with results shown above. However tortuosity is essentially a measure of internal randomness and one would expect the tortuosity fitting factor to compensate for interior morphology differences.

The results of the CO_2 transport tests are remarkable. Due to the larger pore size and decreased sample thickness the transport characteristics of the ITM were expected to be much higher than the CoorsTek sample. This is not the case; both samples show comparable transport characteristics in the configuration tested. The results are especially surprising as the CoorsTek sample is 40% thicker than the ITM sample. While little is known how the transport of the sample scales with thickness, it is clear that the transport characteristics per unit thickness are substantially higher for the CoorsTek Ni-YSZ than for the porous ITM material.

The results of the CO_2 transport can be explained by examining the DGM, equation 4.6 below.

$$\sum_{l\neq k}\frac{[X_l]J_l-[X_k]J_l}{[X_T]D_{kl}^e}+\frac{J_k}{D_{k,Kn}^e}=-\nabla[X_k]-\frac{[X_k]}{D_{k,Kn}^e}\frac{B_g}{\mu}\nabla p \tag{4.6}$$

It can be seen that the species concentration gradient ($\nabla[X_k]$) is determined by three independent driving forces; standard multi-component diffusion ($\sum_{l\neq k}\frac{[X_l]J_l-[X_k]J_l}{[X_T]D_{kl}^e}$), Knudsen diffusion ($\frac{J_k}{D_{k,Kn}^e}$), and pressure driven Darcy flow ($\frac{[X_k]}{D_{k,Kn}^e}\frac{B_g}{\mu}\nabla p$). The effect of each of these driving forces on total mass transport through a given sample can be thought of as a simple resistor circuit shown in Figure 24

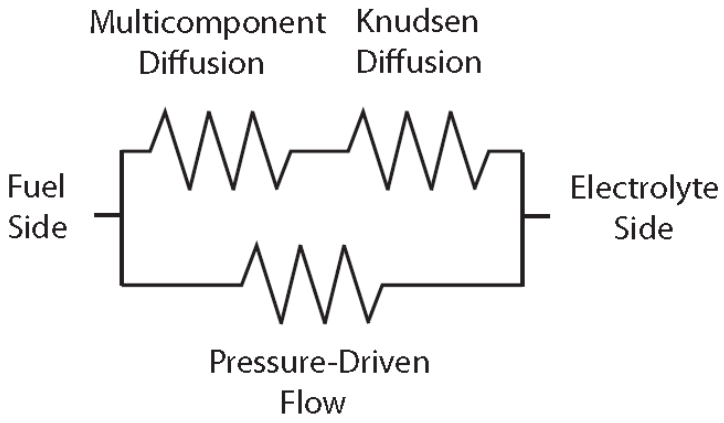

Figure 24 - Illustration of the interactions between flow driving forces as represented by the Dusty Gas Model. Source: (A. Richards, 2011).

Referring to Figure 24 it can be seen that when a high pressure differential is present across the sample (when ∇p is large), the Darcy flow mechanism will dominate the mass transport mechanism. In the SAE the pressure differential is eliminated by balancing the pressure in the fuel side and electrolyte side manifolds. The lack of a pressure differential eliminates the Darcy characteristics from consideration in the overall mass transport performance of the sample. The lack of a Darcy flow component in the transport mechanism of the SAE explains why the ITM sample and the CoorsTek sample transport characteristics are similar. Even though the ITM

sample is thinner, the increased tortuosity and larger particle size of the material impedes the remaining diffusion transport mechanisms.

5.4.3 CH_4 dry reforming results

The CH_4 dry reforming test is performed by supplying the fuel side gas manifold with a mixture of 20% CH_4 and 80% FG. The electrolyte side gas manifold is supplied with a gas mixture of 50% CO_2 and 50% FG. The dry reforming equation is shown below.

$$CH_4 + CO_2 \rightarrow 2CO + 2H_2 \tag{1.10}$$

By comparing the concentration levels of the reforming products (CO and H_2) and reactants (CH_4 and CO_2) in the exhaust gases of the fuel and electrolyte sides, a comparison of the reforming activity of the samples can be made. Figure 25 shows the H_2 and CO concentrations in the fuel and electrolyte exhaust streams of the two samples. Figure 26 shows the reactant (CH_4, CO_2) concentrations remaining in the fuel and electrolyte exhaust streams.

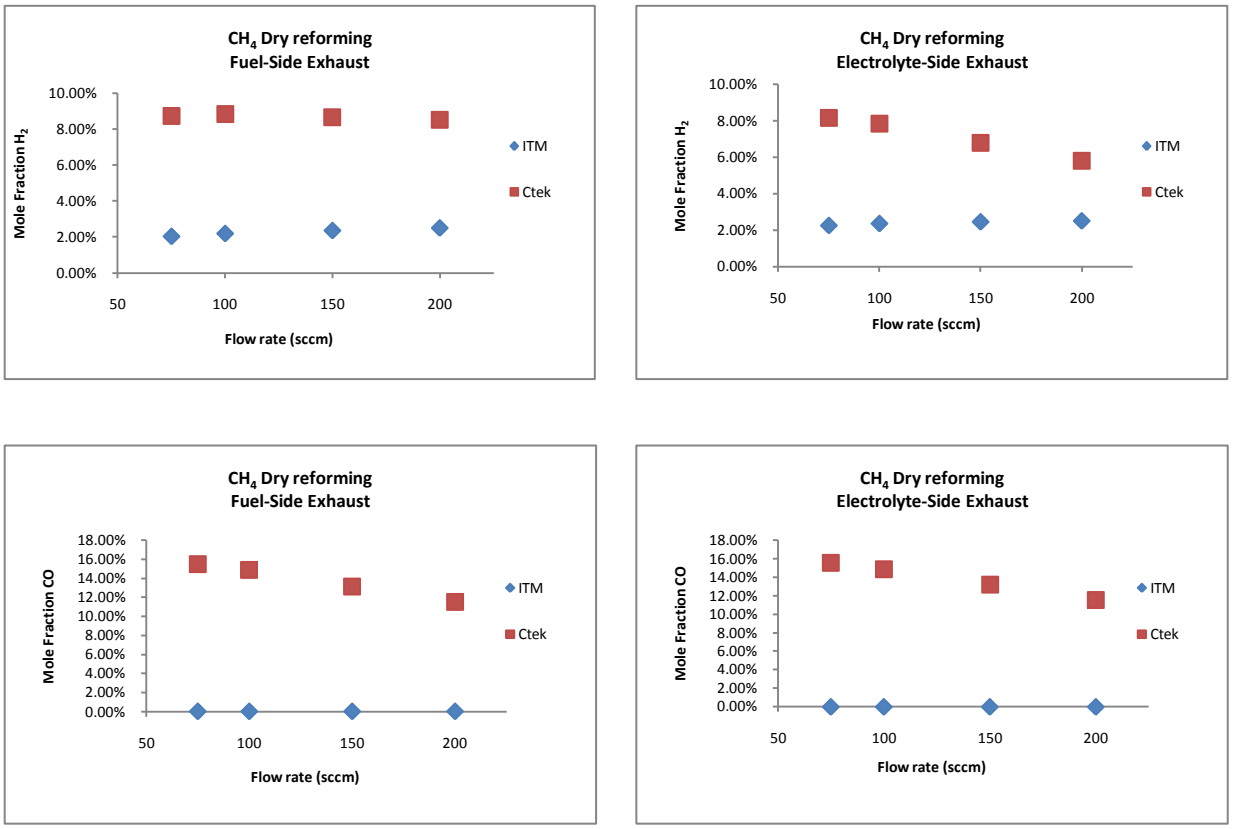

Figure 25 - CH_4 dry reforming – Reforming product exhaust gas concentrations. Top Left: H_2 concentration in fuel-side exhaust. Top Right: H_2 concentration in electrolyte-side exhaust. Bottom Left: CO concentration in fuel-side exhaust. Bottom Right: CO concentration in electrolyte-exhaust

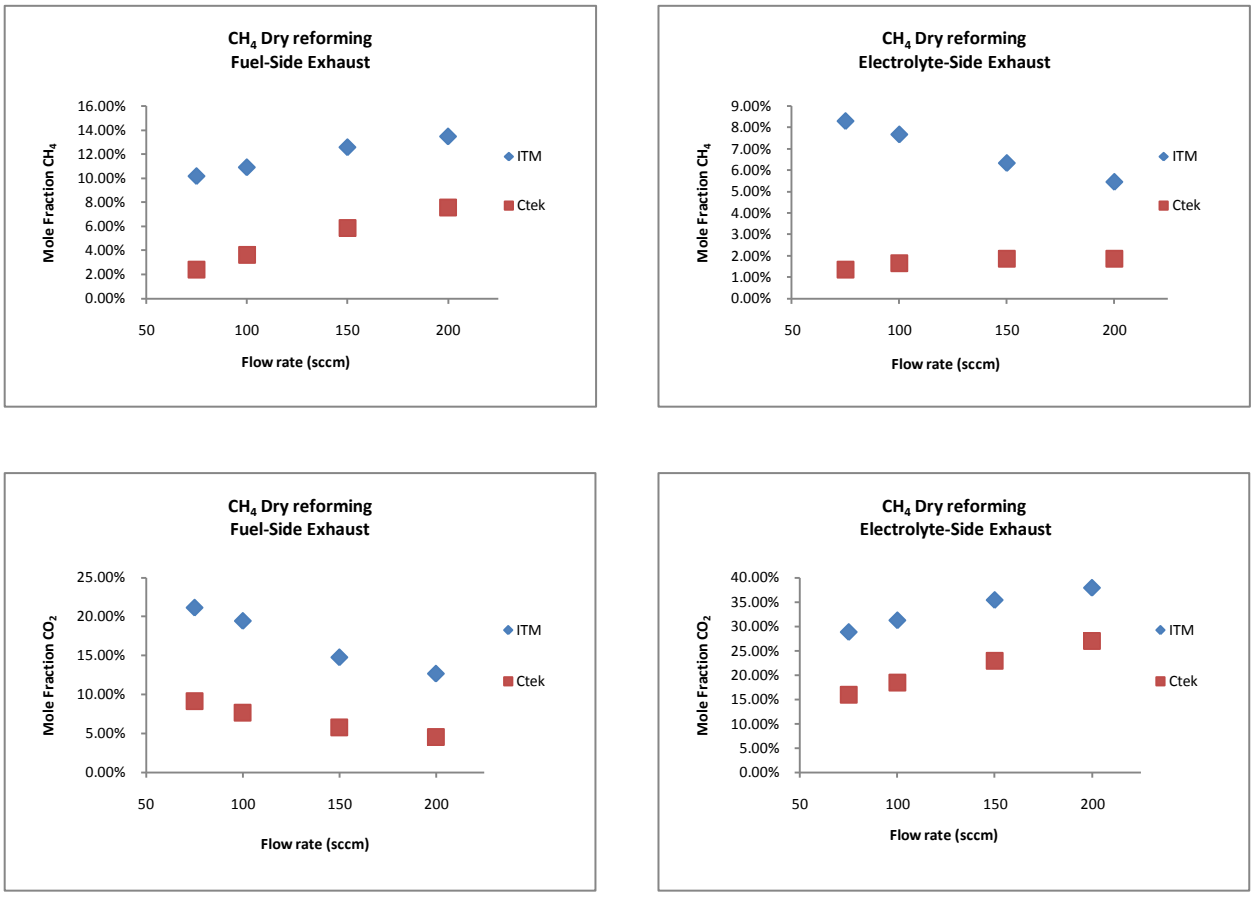

Figure 26 - CH_4 dry reforming – Reforming reactant exhaust gas concentrations. Top Left: CH_4 concentration in fuel-side exhaust. Top Right: CH_4 concentration in electrolyte-side exhaust. Bottom Left: CO_2 concentration in fuel-side exhaust. Bottom Right: CO_2 concentration in electrolyte-exhaust

As can be seen in Figure 25 and Figure 26, reforming product concentrations are higher and reforming reactants are lower in the CoorsTek sample. This implies that the CoorsTek sample is more catalytically active in the reforming reaction. The ITM exhaust stream shows no CO production at all, suggesting that the ITM support is catalytically inert and no dry reforming occurs at the temperature of operation (800C). Low reforming performance of the ITM support was expected, as there is no AFL present to promote the reforming reaction. The fact that the support is completely inert is surprising. Hei et al., Murata et al. and Horita et al. have all demonstrated the reforming capabilities of Fe based catalysts, however all have noted low performance and high susceptibility for coke formation with an Fe based catalyst(M.J. Hei, 1998),(K. Murata, 2004),(T. Horita, 1996).

As the ITM sample is chemically inert during the reforming tests, the reforming test is essentially another mass transport test. The gas mixture applied to the electrolyte side of the sample is the same in both the CO_2 transport test and the reforming test. As such, the CO_2 concentration in the fuel side exhaust of the inert ITM sample during the CO_2 transport test should be comparable to the CO_2 concentration in the fuel side exhaust gas during the dry reforming test. Figure 27 shows the fuel side CO_2 concentrations of the ITM sample for both the CO_2 transport and the reforming tests. As can be seen in the figure, the CO_2 concentrations are a near perfect match, suggesting that the SAE is a highly repeatable experiment.

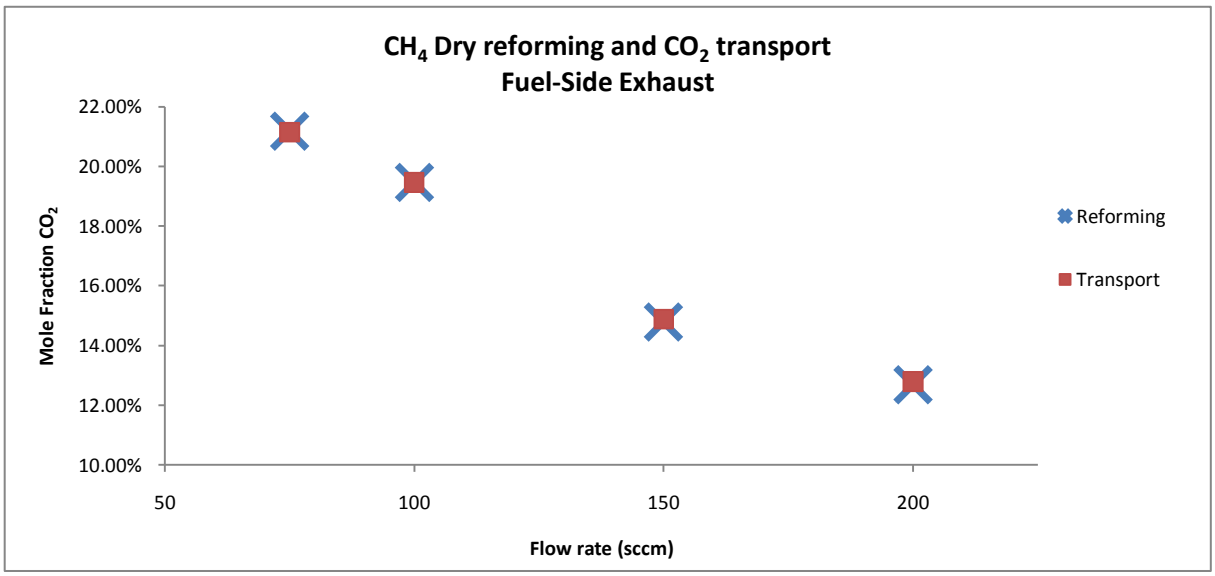

Figure 27- Comparison between fuel side exhaust gas CO_2 concentration of the CO_2 transport and CH_4 reforming tests for the ITM sample. Since the ITM sample is inert during both the CO_2 transport tests and CH_4 reforming tests the fuel side CO_2 concentration should be same for each test.

5.4.4 CH_4 dry reforming model results

The CFCC model is fit to the CH_4 reforming results using the same tortuosity value that was found with the CO_2 transport fit. The model results of the CH_4 reforming test for the CoorsTek and the ITM sample are shown in Figure 28 and Figure 29 respectively.

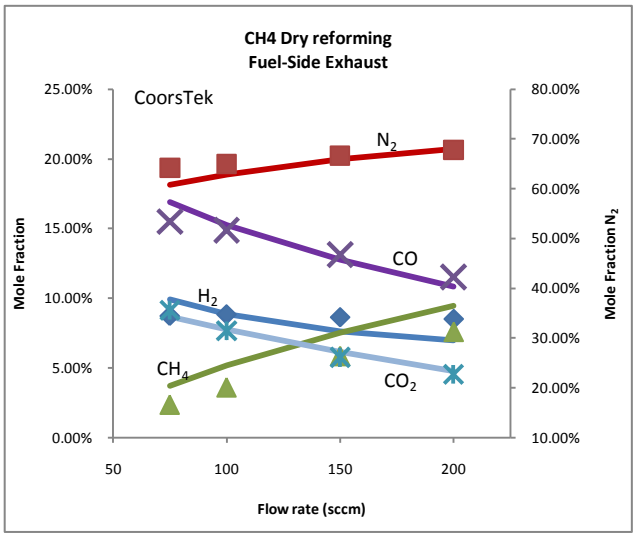

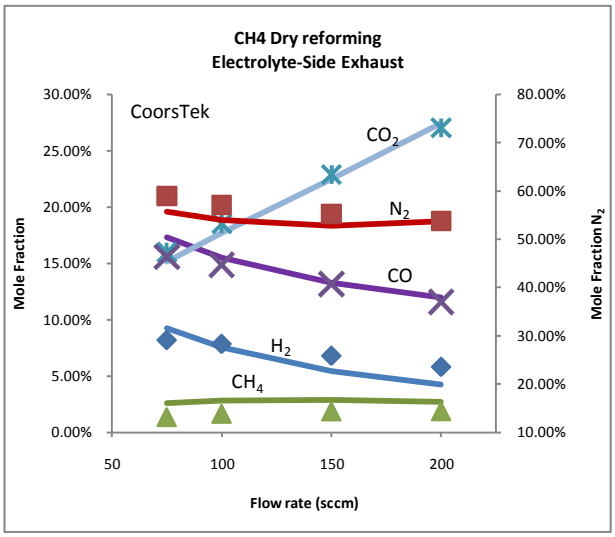

Figure 28- Ni-YSZ CH_4 reforming results – SAE data is represented by data points. Model data is represented by the solid lines. LEFT: Fuel-side exhaust composition RIGHT: Electrolyte-side exhaust composition

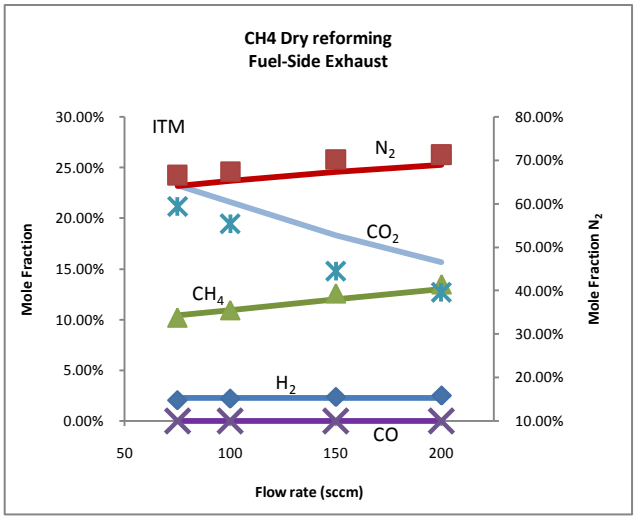

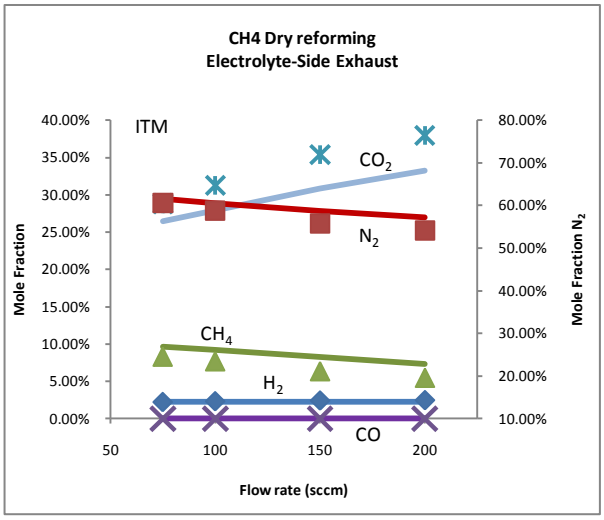

Figure 29- ITM CH_4 reforming results – SAE data is represented by data points. Model data is represented by the solid lines LEFT: Fuel-side exhaust composition RIGHT: Electrolyte-side exhaust composition

Referring to Figure 28 and Figure 29, it is clear that that the CFCC model is a good fit for both the CoorsTek and ITM samples. The fit to the ITM sample is not as good as the fit to the CoorsTek, however the general trends are all correct. The largest discrepancy in the ITM fit is CO_2 concentration, the model predicts approximately 4% higher mole fraction of CO_2 to be

present in the fuel side exhaust than actually seen with SAE experiment. This discrepancy is the same seen with the CO_2 transport results.

6 CONCLUSIONS

The fuel reforming and transport capabilities of two vastly different SOFC anode/support materials have been compared and analyzed. Typically, analysis of these characteristics is done using electrochemical testing procedures, such as polarization measurements and electrochemical impedance spectroscopy. Anode transport and reforming characteristics can only be inferred from these tests because those processes are tightly coupled with the electrochemical reactions in an active fuel cell. Using the unique Separated Anode Experiment at the CFCC it is possible to decouple these processes and directly measure the transport and reforming characteristics of the anode structure with no need for electrochemical activity. Using the SAE, a leading, commercially developed, Ni-YSZ SOFC anode was used as baseline to compare the mass transport and reforming reaction kinetics present within a leading porous metal support. The commercially developed CoorsTek reaction sintered Ni-YSZ anode was used as baseline in this study. The CoorsTek Ni-YSZ anode has been previously evaluated by Storjohann et al, and constitutes the state-of-the-art in ceramic Ni-YSZ anode design(D. Storjohann, 2009). A porous metal support developed by Plansee SE specifically for SOFC support applications (Plansee porous ITM support) serves as the experimental group.

The Ni-YSZ anode shows significant reforming characteristics while the ITM sample showed no catalytic activity to reforming. It is not surprising that the Ni-YSZ anode showed substantially higher reforming characteristics than the ITM sample because the ITM sample lacked a functional layer to catalyze the dry reforming reaction. While the ITM sample's reforming capabilities were expected to be substantially less than the Ni-YSZ anode, the ITM sample was not expected to be completely inert to reforming. Methane reforming over Fe based catalysts has been documented in multiple studies (T. Horita, 1996),(M.J. Hei, 1998),(K. Murata, 2004).

SEM analysis of the two samples showed vastly different morphologies. The ITM sample has significantly larger particle and pore size than the Ni-YSZ anode. With the vast differences in morphology, the mass transport characteristics of the samples were expected to be vastly different. Surprisingly, the Ni-YSZ and ITM samples show comparable mass transport characteristics. This can be explained by the lack of a pressure differential across the sample while being tested. Large pore sizing promotes increased transport through porous media by increasing the pressure driven Darcy flow characteristics of the material. Darcy flow is driven by a pressure differential across the material. In the SAE, pressure differential across the

sample is minimized to accurately represent the SOFC operating environment. As the pressure differential is minimized the Darcy flow characteristics of the sample have little to no effect on the mass transport in SOFC operating conditions.

Visual and SEM comparisons for the ITM material pre and post testing in the SAE show that the ITM sample developed an oxide scale while being tested at SOFC operating temperature. However, it is unclear whether this scale is the desirable continuous Cr_2O_3 scale or a combination of Cr_2O_3 and the detrimental Fe_2O_3. An oxidation study of porous ITM substrate has been conducted by Franco et al. with a generally positive result (T. Franco, 2009). Neither composition of the oxide scale nor ASR measurements were reported, which makes it difficult to predict the operational lifetime expectancy of the substrate.

7 WORKS CITED

A. Bautista, E.A.F.V.C.M.a.R.C., 2008. Oxidation behavior of Highly Porous Metallic Components. *Oxidation of Metals*, 70, pp.267-86.

A. Mineshige, K.F.S.O.T.K.M.K.T.Y.K.K.M.I.Z.O., 2006. Porous metal tubular support for solid oxide fuel cell design. *Electrochemcial and Solid State Letters*, 9, pp.A427-29.

A. Richards, N.S.R.K.H.Z., 2010. Internal Reforming Chemistry in Novel SOFC Anodes and Architectures. In *Proceedings of the 9th European Solid Oxide Fuel Cell Forum*. Lucerne, Switzerland, 2010.

A. Richards, N.S.R.K.M.M.S.B., 2011. Gas Transport and Internal Reforming Chemistry in SOFC Anode Supports and Structures. In *SOFC XII*. Montreal, 2011.

ATI Allegheny Ludlum, 2007. [Online] Available at: http://www.brownmetals.com/downloads/AlloyEbriteTechSheet.pdf.

Atkinson, A., 1985. Transport processes during the growth of oxide films at elevated temperature. *Reviews of Modern Physics*, 57(2), pp.437-70.

C. Hwang, C.-H.T.C.-H.L.C.-H.S., 2008. Plasma sprayed metal supported YSZ/Ni-LSGM-LSCF. *Journal of Power Sources*, 180, pp.132-42.

D. Morgensen, J.-D.G.P.V.H.K.D.-J.J.U.N., 2011. Internal steam reforming in solid oxide fuel cells: status and opertunities of kinetic studies and thier impact on modelling. *Journal of Power Sources*, 196, pp.25-38.

D. Storjohann, J.D.N.P.S.H.Z.R.J.K.S.M.D.B., 2009. Fabrication and evaluation of solid-oxide fuel cell anodes employing reaction-sintered yttria-stabilized zirconia. *Journal of Power Sources* , 193, pp.706-12.

Daggett, J.M., 2008. *Ethanol transport and chemistry in Ni/YSZ anodes for solid oxide fuel cell applications.* Master's thesis. Golden, CO: Colorado School of Mines.

E. Hecht, G.K.G.H.Z.A.M.D.R.J.K.L.M.a.O.D., 2005. Methane reforming kinetics within Ni-YSZ SOFC anode support. *Applied Catalysis A*, 295, pp.40-51.

E. Ruckenstein, Y.H.H., 1995. Carbon dioxide reforming of Methane over nickel/ alkaline earth oxide catayst. *Applied Catalysis A: General*, 133, pp.149-61.

G.K. Gupta, E.S.H.H.Z.A.M.D.a.R.J.K., 2006. Gas-Phase Reactions of Methane and Natural-Gas with Air and Steam in non-catalytic regions of a solid-oxide fuel cell. *Journal of Power Sources*, 156, pp.434-47.

Gupta, G.K., 2007. *Analysis of gas-phase and catalytic kinetics in solid oxide fuel cells.* PhD thesis. Golden, CO: Colorado School of Mines.

H. Sumi, Y.-H.L.H.M.T.M.a.K.E., 2010. Comparison Between Internal Steam and CO2 Reforming of Methane for Ni-YSZ and Ni-ScSZ SOFC Anodes. *Journal of The Electrochemical Society*, 157, pp.1118-25.

H. Zhu, R.J.K.V.M.J.O.D.a.D.G.G., 2005. Modeling elementary heterogeneous chemistry and electrochemistry in solid-oxide fuel cells. *Journal of The Electrochemical Society*, 152, pp.A2427-40.

H. Zhu, D.G.G.R.J.K., 2005. Solid-oxide fuel cells with hydrocarbon fuels. *Proceedings of the Combustion Institute*, 30, pp.2379-404.

H.J. Cho, G.M.C., 2009. Frabrication and characterization of Ni-supported solid oxide fuel cell. *Solid State Ionics*, 180.

Hansen, J.R.R.-N.a.J.-H.B., 1993. CO2-Reforming of Methane over Transition Metals. *Journal of Catalysis* , 144, pp.38-49.

Haynes International, 1997. [Online] Available at: http://www.haynesintl.com/pdf/h3009.pdf.

Haynes International, 2007. [Online] Available at: http://www.haynesintl.com/230HaynesAlloy.htm.

Hecht, E., 2005. *Internal reforming of methane in a nickel-yttria stabilized zirconia solid oxide fuel cell anode.*. Master's thesis. Golden, CO: Colorado School of Mines.

I. Antepara, I.V.L.M.R.N.L.U.C.A.L., 2005. Evaluation of Ferritic steels for use as interconnects and porous metal supports in IT-SOFCs. *Journal of Power Sources*, 151, pp.103-07.

I. Antepara, M.R.I.V.N.B.F.C., 2010. Influence of Different Aspects of the SOFC Anode Environment on the Oxidation Behavior of Porous Samples Made of Crofer. *Journal of Fuel Cell Science and Technology*, 7, pp.1-7.

J. H. Zhu, S.J.G.Z.G.L.a.W.D.P., 2007. Evaluation of Binary Fe-Ni Alloys as Intermediate-Temperature SOFC Interconnect. *Journal of the Electrochemical Society*, 154, pp.1288-94.

J. Sfeir, P.A.B.P.M.N.X.R.V.J.J.M.J.V.h.K.R.T., 2001. Lanthanum chromite based catalysts for oxidation of methane directly on SOFC anodes. *Journal of Catalysis* , 202, pp.229-44.

J.-M. Klein, M.H.P.G.Y.B.a.S.G., 2008. A Solid Oxide Fuel Cell Operating in Gradual Internal Reforming Conditions under Pure Dry Methane. *Electrochemical and Solid-State Letters*, 11(8), pp.B144-47.

J.-M. Klein, M.H.C.R.Y.B.S.G., 2009. Direct methane solid oxide fuel cell working by gradual internal steam reforming: Analysis of operation. *Journal of Power Sources*, 193, pp.331-37.

J.R. Rostrup-Nielsen, J.-H.B.H., 1993. CO2-Reforming of Methane over Transisiton Metals. *Journal of Catalysis*, 144, pp.38-49.

J.R. Rostrup-Nielsen, J.B.H.S.H.N.C.A.-K.J., 2006. Sites for catalysis and electrochemistry in solid oxide fuel cell (SOFC) anode. *Applied Physics A*, 85, pp.427-30.

J.W. Jan, H.M.M.E.T.I., 2005. High-power SOFC using LSGM-SDC composite film. *Electrochemical and Solid State Letters*, 8(8), pp.A389-91.

Jefferson Lab, 2010. *Jefferson Lab Science Education*. [Online] Available at: http://education.jlab.org/itselemental/ele001.html.

K. Murata, L.W.M.S.M.I.I.T.N.M., 2004. Hydrogen Production from Steam Reforming of Hydrocarbons over Alkaline-Earth-Modified Fe - or Ni-Based Catalysts. *Energy & Fuels*, 18, pp.122-26.

K. Tomishige, M.N.K.M.K.K., 2004. Effect of oxygen addition to steam and dry reforming of methane on bed temperature profile over Pt and Ni catalysts. *Fuel Processing Technology*, 85, pp.1103-20.

L. Rose, O.K.C.D.-P.T.R.M., 2009. Characterization of Porous Stainless Steel 430 for Low- and Intermediate-Temperature Solid Oxide Fuel Cell Substrates. *International Journal of Green Energy*, 6, pp.638-45.

M. Pillai, Y.L.H.Z.R.J.K.a.S.A.B., 2010. Stability and coking of direct-methane solid oxide fuel cells. *Journal of Power Sources*, 195, pp.271-79.

M.C. Tucker, H.K.C.P.J.J.C.D.J.S.J.V., 2006. A fundamental study of chromium deposition on solid oxide fuel cell cathode materials. *Journal of Power Sources*, 160, pp.130-38.

M.J. Hei, H.B.C.J.Y.Y.J.L.Y.Z.L.G.W.D.W.L., 1998. CO2 reforming of methane on transition metal surfaces. *Surface Science*, 417, pp.82-86.

Malinauskas, E.M.a.A., 1983. *Gas Transport in Porous Media: The Dusty Gas Model*. New York: American Elsevier.

Micromeritics Instrument Corporation, 2010. [Online] Available at: http://www.micromeritics.com/Repository/Files/Mercury_Porosemitry_Theory_poster_.pdf.

N. Oishi, Y.Y., 2010. Evaluation of Metal Supported Ceria Based Solid Oxide Fuel Cell Fabricated by Wet Powder Spray and Sintering. *Journal od the Electrochemical Society*, 157(1), pp.B125-29.

N.P Brandon, D.J.B., 2006. Engineering porous materials for fuel cell applications. *Philosophical Transactions of The Royal Society A*, 364, pp.147-59.

N.P. Brandon, A.B.D.C.D.C.A.D.K.E.-K.e.a., 2004. Development of Metal Supported Solid Oxide Fuel Cells for Operation at 500-600 C. *Journal of Fuel Cell Science and Technology*, 1, pp.61-65.

N.P. Brandon, D.C.D.C.A.D.K.E.-K.D.H.R.L.G.L.N.M.T.M.R.T.A.S.a.M.S., 2004. Development of Metal Supported Solid Oxide Fuel Cells for Operation at 500-600C. *Journal of Materials Engineering and Performance*, 13(3), pp.253-56.

P. Szabo, J.A.T.F.M.G.A.R.A.Z.A.A., 2009. Progress in Metal Supported Solid Oxide Fuel Cells and Stacks for APU. *ECS Transactions*, 25(2), pp.175-85.

P.K. Cheekatamarla, C.M.F.a.J.C., 2008. Internal reforming of hydrocarbon fuels in tubular solid oxide fuel cells. *International Journal of Hydrogen Energy*, 33, pp.1853-58.

Plansee SE, 2010. *Plansee corporate website*. [Online] Available at: http://www.plansee.com/news-2393.htm.

Q-A. Huang, B.W.W.Q.R.H., 2009. Impedance diagnosis of metal-supported SOFCs with SDC as electrolyte. *Journal of Power Sources*, 191, pp.297-303.

R. Hui, J.O.B.D.-P.W.Q.S.Y.J.-G.L.C.M., 2009. High performance metal-supported solid oxide fuel cell fabricated by thermal spray. *Journal of Power Sources*, 191, pp.371-76.

R. O'Hayre, S.W.C.W.C.F.P., 2008. *Fuel Cell Fundamentals*. 2nd ed. Hoboken, New Jersey, USA: John Wiley & Sons.

R.J. Kee, M.E.C.a.P.G., 2003. *Chemically Reacting Flow: Theory and Practice*. Hoboken, NJ: John Wiley.

Richards, A., 2010. *A unique experimental tool for the evaluation of gas transport and internal-reforming chemistry within solid oxide fuel cell anodes*. Master's thesis. Golden, CO: Colorado School of Mines.

Richards, A., 2010. *A Unique Experimental Tool for the Evaluation of Gas Transport and Internal-Reforming Chemistry within Solid Oxide Fuel Cell Anodes*. Master's Thesis. Golden, CO: Colorado School of Mine.

Richards, A., 2010. *Gas Transport and Internal Reforming Chemistry in SOFC Anode supports and Structures*. PhD Thesis proposal. Golden CO: Colorado School of Mines.

S. Fontana, R.A.S.C.P.P.G.C.M.V.R.M.M.S., 2007. Mettallic interconnects for SOFC: Characterization of corrosion resistance and conductivity evaluation at operating temperature of differently coated alloys. *Journal of Power Sources*, 171, pp.652-62.

S. Molin, B.K.M.G.a.P.J., 2008. Evaluation of porous 430L stainless steel for SOFC operation at intermediate temperatures. *Journal of Power Sources*, 181, pp.31-37.

S. Molin, M.G.B.K.P.J., 2009. Evaluation of 316L porous stainless steel for SOFC support. *Journal of the European Ceramic Society*, 29, pp.757-62.

S. Molin, M.G.a.P.J., 2010. High temperature oxidation of porous alloys for solid oxide fuel cell applications. *Solid State Ionics*, 181, pp.1214-20.

Song, C., 2002. Fuel processing for low-temperature and high-temperature fuel cells Challenges, and oppertunities for sustainable development in the 21st century. *Catalysis Today*, 77, pp.17-49.

Steele, B.C.H., 2000. Appraisal of CGO electrolytes for IT-SOFC operation at 500C. *Solid State Ionics* , 129, pp.95-110.

T. Franco, K.S.Z.I.G.S.a.A.V., 2007. Ceramic Diffusion Barrier Layers for Metal Supported SOFCs. *ECS Transactions*, 7(1), pp.771-80.

T. Franco, M.B.M.R.G.K.A.V.a.L.S.S., 2009. Recent Development Aspects of Metal Supported Thin-Film SOFC. *ECS Transactions*, 25(2), pp.681-88.

T. Horita, N.S.T.K.H.Y.a.M.D., 1996. Oxidation and Steam Reforming of CH4 on Ni and Fe Anodes under Low Humidity Conditions in Solid Oxide Fuel Cells. *Journal of the Electrochemical Society*, 143(4), pp.1162-68.

T. Ishihara, H.M.a.Y.T., 1994. Doped LaGaO3 Perovskite Type Oxide as a New Oxide Conductor. *Journal of the American Chemical Society* , 116(9), pp.3801-03.

T. Ishihara, J.Y.M.S.H.M., 2006. Ni-Fe bimetallic anode as an active anode for intermediate temperature SOFC using LaGaO3 based electrolyte film. *Electrochimica Acta*, 52, pp.1645-50.

T. Ishihara, J.Y.M.E.S.O.H.M., 2008. Ni-Fe Alloy-Supported Intermediate Temerature SOFCs Using LaGaO3 Electrolyte Film for Quick Startup. *Journal of Fuel Cell Science and Technology*, 5, pp.1-3.

ThyssenKrupp VDM, 2005. [Online] Available at: http://www.thyssenkrupp-vdm-fareast.com/media/down_datasheets_heatres_new/crofer22apu_e.pdf.

Tucker, M.C., 2010. Progress in metal-supported solid oxide fuel cells: A review. *Journal of Power Sources*, 195, pp.4570-82.

United States Department of Energy, 2008. *Hydrogen Production*. [Online] Available at: https://www1.eere.energy.gov/hydrogenandfuelcells/production/natural_gas.html.

unknown, 2011. *Bloomberg Businessweek*. [Online] Available at: http://investing.businessweek.com/research/stocks/private/snapshot.asp?privcapId=61567383.

W.G.Coors, R.S., 2007. *Preparation of yttria-stabilized zirconia reaction sintered products.* Patent Number: 20070176332. United States of America.

W.Z. Zhu, S.C.D., 2003. A review on the status of anode materials for solid oxide fuel cells. *Materials Science and Engineering A*, A362, pp.228-39.

Y. Lin, Z.Z.S.A.B., 2006. Improving the stability of direct-methane solid oxide fuel cell using anode barrier layers. *Journal of Power Sources* , 158, pp.1313-16.

Y. Matsuzaki, I.Y., 2000. The poisoning effect of sulfur-containing impurity gas on a SOFC anod: Part I. Dependence on temperature, time, and impurity concentration. *Solid State Ionics*, 132, pp.261-69.

Y.-S. Chou, J.W.S.L.A.C., 2002. Ultra-low leak rate of hybrid compressive mica seals for solid oxide fuel cells. *Journal of Power Sources* , 112, pp.130-36.

Z. Wang, J.O.B.S.Y.C.D.-P.W.Q.R.H.R.M.D.G., 2008. Dynamic evaluation of low-temperature metal-supported solid oxide fuel cell oriented to auxiliary power units. *Journal of Power Sources*, 176, pp.90-95.

Z. Zhan, S.A.B., 2005. An octane-fueled solid oxide fuel cell. *Science*, 308, pp.844-47.